

A SPECTROPHOTOMETRIC SURVEY OF *K*-BAND EMISSION LINES IN PLANETARY NEBULAE

LAUREN LIKKEL,^{1,2} HARRIET L. DINERSTEIN,³ DAN F. LESTER,³ ANNA KINDT,^{1,2} AND KEVIN BARTIG^{1,2}

Received 2005 September 12; accepted 2005 November 22

ABSTRACT

We present observations of 16 planetary nebulae (PNs) in the 2 μm (*K* band) spectral region, obtained with a long-slit near-infrared spectrometer at McDonald Observatory. In general, the strongest features in our spectra are recombination lines of H I, He I, and (in some cases) He II. Half the sample shows emission from vibrationally excited H₂. Some of the observed PNs (e.g., M 1-13) display H₂ line ratios characteristic of shocked, thermalized gas, while others (e.g., BD +30 3639) have ratios intermediate between pure radiative (UV) and shock excitation, consistent with either a combination of the mechanisms or UV illumination of dense material. Our spectra of J900 and M 1-13 confirm that published narrowband images trace the H₂ emission, and we find that the H₂ emission in SwSt 1 has a larger spatial extent than previously reported. In IC 5117, SwSt 1, and NGC 40 we detect the [Kr III] 2.199 μm line identified by Dinerstein in 2001, with strengths indicating that krypton is enriched relative to the solar abundance, most markedly so in NGC 40. We also detect several lines from the ³G term of [Fe III] in Vy 2-2, SwSt 1, and marginally in Cn 3-1. The [Kr III] and [Fe III] lines fall near in wavelength to H₂ transitions, which are often used as diagnostics for UV excitation because they arise from higher vibrationally excited levels ($v = 2, 3$). For moderate spectral resolving power, $R \leq 600$, these lines may be blended with, or even mistaken for, the corresponding H₂ lines, leading to misinterpretation of the H₂ emission. The strength of both the Kr and Fe nebular emission lines can be enhanced by special circumstances, Kr because of nucleosynthetic self-enrichment in the progenitor star and Fe due to inefficient initial dust condensation or partial destruction of the dust after formation, causing a larger fraction of the elemental iron to reside in the gas phase.

Key words: infrared: ISM — planetary nebulae: general — planetary nebulae: individual (BD +30 3639, IC 5117, J900, M 1-13, NGC 40, SwSt 1, Vy 2-2, IC 2003)

1. INTRODUCTION

Observable quantities of molecules are present in some planetary nebulae (PNs) despite the fact that the PN material is subjected to the central star's strong UV radiation field, which is capable of dissociating and ionizing the gas. The survival of molecules in PNs can be attributed to several factors, including time-dependent effects arising from the rapid evolution of the central star and location of the molecules in dense regions where they are shielded from the dissociating radiation. Relevant time-dependent effects include the recent onset of the dissociating radiation field for young PNs (e.g., Goldshmidt & Sternberg 1995; Hollenbach & Natta 1995) and luminosity fading of the central star for some older PNs (Tylenda 1986; Blöcker 1995). Regions that may shelter molecules for long time periods include the dense equatorial tori of bipolar nebulae (Kastner et al. 1996; Guerrero et al. 2000) or the interiors of clumps or globules (Tielens 1993; Redman et al. 2003). It may even be possible for molecular reformation processes (on grain surfaces and/or via gas-phase reactions) to maintain an observable molecular fraction in competition with photodissociation (Hasegawa et al. 2000; Hasegawa 2003; Aleman & Gruenwald 2004). Evolutionary models for the neutral envelopes of PNs predicting that molecular emission may be observable for several thousand years (Natta & Hollenbach 1998) are confirmed by observations of CO and H₂ emission in relatively evolved PNs such as the Helix and Ring Nebulae (Huggins et al. 2002; O'Dell et al. 2002; Speck et al. 2003).

The most cosmically abundant molecule, H₂, is also the most widely detected one. Its near-infrared quadrupole emission lines have been seen in over 60 PNs and proto-planetary nebulae (PPNs), objects that have not yet fully reached the PN stage. (However, the distinction between PNs and PPNs is problematic and often inconsistent, with PPNs sometimes essentially *defined* as objects with molecular emission; see the discussion by Dinerstein [2004a].) The most commonly observed transitions lie in the 2 μm spectral region (*K* band) and originate from vibrationally excited levels of the ground electronic state. The $v = 1-0$ S(1) 2.122 μm line is particularly favored for imaging surveys because it is strong and relatively free of telluric interference. The first few excited vibrational states can be populated by collisional excitation in gas heated by low-velocity shocks or by fluorescent pumping via the absorption of UV photons followed by a radiative cascade. In principle one can distinguish between these two possibilities from the line intensity ratios, since radiative excitation produces an emergent spectrum with many lines from high energy levels ($v \geq 3$) that are absent for thermal excitation (e.g., Black & van Dishoeck 1987). Unfortunately, it is not so easy to discriminate between the two mechanisms in practice, because a radiative spectrum can be modified by effects that cause it to mimic collisional excitation. This can happen, for example, if the UV-illuminated gas is very dense ($n \gtrsim 10^4 \text{ cm}^{-3}$; e.g., Sternberg & Dalgarno 1989) or if the radiation field includes X-rays that heat the gas so strongly that collisional excitation overwhelms the initially nonthermal population distribution (Maloney et al. 1996; Vicini et al. 1999).

The early detections of H₂ emission in PNs, mostly from observations with relatively low spectral resolving power that could not resolve many individual lines, were generally ascribed to shock excitation (e.g., Zuckerman & Gatley 1988). The paradigm shift to interpreting the H₂ as being primarily radiatively excited, in a “photodissociation region” or PDR, was prompted by the

¹ Department of Physics and Astronomy, University of Wisconsin, Eau Claire, WI 54702-4004; likkel@uwec.edu.

² Visiting Astronomer, McDonald Observatory, University of Texas at Austin, 1 University Station C1402, Austin, TX 78712-0259.

³ Department of Astronomy, University of Texas at Austin, 1 University Station C1400, Austin, TX 78712-0239; harriet@astro.as.utexas.edu, dfl@astro.as.utexas.edu.

TABLE 1
OBSERVING LOG FOR PRIMARY SETUP (2.095–2.260 μm)

Nebula	PNG Number	Observation Date	Aperture ^a (arcsec)	Integration Time ^b (minutes)	Conditions
NGC 40.....	120.0+09.8	2000 Nov 24	1.8×8.6^c	36	Variable
M 1-4.....	147.4–02.3	2000 Nov 24	1.8×8.6	48	Partly cloudy
IC 2003.....	161.2–14.8	2000 Nov 23	1.8×15.5	80	Clear, windy
IC 2165.....	221.3–12.3	1999 Nov 16	1.8×8.6	52	Clear
J900.....	194.2+02.5	1999 Nov 15	1.8×10.8^d	56	Clear
M 1-6.....	211.2–03.5	1999 Nov 16	1.8×6.5	100	Clear
M 1-13.....	232.4–01.8	2000 Nov 20	1.8×18.0	56	Partly cloudy
M 1-13.....	232.4–01.8	2000 Nov 22	1.8×18.0	72	Partly cloudy
Me 2-1.....	342.1+27.5	2000 Jul 21	1.8×10.8	46	Clear
NGC 6210.....	043.1+37.7	2000 Jun 26	1.8×10.8	52	Partly cloudy
Vy 1-2.....	053.3+24.0	2000 Jun 27	1.8×8.6	60	Cirrus
SwSt 1.....	001.5–06.7	2000 Jul 22	1.8×6.5	24	Clear
Cn 3-1.....	038.2+12.0	2000 Jul 20	1.8×7.2	32	Cirrus
Vy 2-2.....	045.4–02.7	2000 Jun 27	1.8×8.6	40	Cirrus
BD +30 3639.....	064.7+05.5	2000 Jul 22	1.8×10.1^c	14	Clear
IC 5117.....	089.8–05.1	2000 Nov 22	1.8×8.6	16	Clear
IC 5217.....	100.6–05.4	2000 Nov 24	1.8×8.6	80	Clear

^a Unless otherwise indicated, the aperture was centered on the optical nebula with the long axis oriented east-west.

^b Effective on-source integration time.

^c Spectra from western and eastern arcs; slit offset 7".4 north of the central star.

^d Slit position angle rotated to 130° to align with the nebular major axis.

^e Extraction aperture extends from 3".6 to 13".6 due east of the central star.

discovery of a pure fluorescent H₂ emission spectrum in the PN Hubble 12 (Dinerstein et al. 1988; Ramsay et al. 1993; Luhman & Rieke 1996). The current consensus is that radiative excitation usually dominates, but a variety of behaviors is seen, with some objects (PNs and PPNs) exhibiting line ratios closer to the shock case (Hora et al. 1999, hereafter HLD99; Lumsden et al. 2001a, hereafter LPH01). PPNs, which have less evolved central stars (Hrivnak 2003), are more likely to have shock-dominated H₂ spectra than bona fide PNs (García-Hernández et al. 2002; Davis et al. 2003), possibly due to the presence of stronger winds in this phase of evolution, as well as the fact that their stellar radiation fields have fewer energetic UV photons. On the other hand, the uncertainty about the excitation mechanism makes it difficult to evaluate the actual fraction of true PNs with significant molecular content. This is exacerbated by the fact that fluorescence is intrinsically less efficient than collisional excitation, introducing a bias in favor of preferentially detecting shock-excited over radiatively excited H₂. These issues motivated us to undertake the present study, an attempt to clarify the excitation mechanism for H₂ by expanding the sample of PNs with well-studied *K*-band spectra.

In this paper we present *K*-band spectrophotometric observations of 16 compact northern PNs, 8 of which display H₂ emission, and discuss the constraints that these measurements place on the excitation mechanism(s). We also discuss other features in the spectra, including collisionally excited lines of [Fe III] and [Kr III] that are not usually considered to be significant in the spectra of PNs. The confusion of these lines with several key H₂ transitions can lead to misinterpretation of the H₂ spectrum, a potentially serious effect, since these ionic lines can be significantly enhanced in particular PNs due to chemical enrichment or a dust deficiency.

2. OBSERVATIONS AND REDUCTIONS

We obtained spectra of our targets in the region ~ 2.0 – $2.3 \mu\text{m}$ using CoolSpec (Lester et al. 2000), a modular long-slit near-infrared spectrometer, at the Cassegrain focus of the 2.7 m Harlan J. Smith telescope at McDonald Observatory. This sur-

vey was conducted over the period 1998–2000, and several objects were observed multiple times. For each object, we present here the data with the highest signal-to-noise ratio (S/N), generally from the more recent observing sessions. Observing logs are given in Tables 1 and 2. The detector was a NICMOS3 HgCdTe 256×256 pixel array. We used a $430 \mu\text{m}$ entrance slit ($1''.8$ on the sky) and a grating with 75 lines mm^{-1} in second order, yielding a spectral resolving power of $R \sim 700$ ($\sim 30 \text{ \AA}$) for a point source. The pixel size corresponded to $0''.36$ in the spatial direction. The $\sim 90''$ slit length enabled us to estimate the angular extent of the emitting regions and tailor the dimensions of the extraction aperture accordingly; the cross-dispersion length of each aperture is listed in Tables 1 and 2. The slit was oriented east-west, except for J900, for which we rotated the position angle in order to align the long axis of the slit with the source structure (see § 3.4.7).

The data reductions were performed with IRAF.⁴ Time-adjacent off-source positions were subtracted in order to remove

TABLE 2
OBSERVING LOG FOR SUPPLEMENTAL SETUP (1.975–2.145 μm)

Nebula	Observation Date	Aperture ^a (arcsec)	Integration Time ^b (minutes)	Conditions
M 1-13.....	2000 Nov 22	1.8×18.0^c	116	Partly cloudy
Vy 2-2.....	2000 Jun 27	1.8×8.6	24	Cirrus, humid
IC 5117.....	2000 Nov 23	1.8×10.8	20	Clear

^a Unless otherwise indicated, the aperture was centered on the optical nebula with the long axis oriented east-west.

^b Effective on-source integration time.

^c Slit positioned so that the long axis cut across the “waist” of this bipolar nebula.

TABLE 3
FLUXES FOR BRIGHT LINES (FULL SAMPLE)

Nebula (1)	$F_{\text{Br}\gamma}$ (2)	$F(\text{He I})/F_{\text{Br}\gamma}$ (2.113/2.166) (3)	$F(\text{He II})/F_{\text{Br}\gamma}$ (2.189/2.166) (4)	$F(\text{H}_2)/F_{\text{Br}\gamma}$ (2.122/2.166) (5)	Ions Seen (6)
NGC 40 W.....	12.2 ± 0.3	≤0.03	≤0.017	0.058 ± 0.007	[Kr III]
NGC 40 E.....	4.95 ± 0.1	≤0.04	≤0.04	≤0.04	[Kr III]
M 1-4.....	14.5 ± 0.5	0.041 ± 0.008	≤0.021	≤0.021	...
IC 2003.....	110 ± 0.2	0.082 ± 0.018	0.232 ± 0.013	0.053 ± 0.010	...
IC 2165.....	33.0 ± 0.6	0.097 ± 0.025	0.15 ± 0.02	≤0.03	...
J900.....	25.7 ± 1.2	≤0.06	0.175 ± 0.028	0.148 ± 0.022	...
M 1-6.....	36.0 ± 1.0	0.033 ± 0.009	≤0.07	≤0.07	...
M 1-13.....	3.6 ± 0.1	≤0.08	≤0.060	1.68 ± 0.10	...
Me 2-1.....	6.1 ± 0.2	≤0.05	0.26 ± 0.04	≤0.05	...
NGC 6210.....	169 ± 2	0.045 ± 0.004	≤0.008	≤0.007	...
Vy 1-2.....	12.5 ± 0.3	0.07 ± 0.01	0.100 ± 0.014	≤0.03	...
SwSt 1.....	210 ± 5	0.039 ± 0.005	≤0.007	0.057 ± 0.005	[Kr III], [Fe III]
Cn 3-1.....	42 ± 1	0.024 ± 0.007	≤0.012	≤0.015	[Fe III]?
Vy 2-2.....	65 ± 3	0.070 ± 0.005	≤0.006	0.032 ± 0.004	[Fe III]
BD +30 E.....	9.5 ± 0.5	0.084 ± 0.025	≤0.077	0.73 ± 0.06	...
IC 5117.....	95 ± 0.5	0.089 ± 0.005	0.048 ± 0.004	0.097 ± 0.005	[Kr III]
IC 5217.....	18.1 ± 0.2	0.064 ± 0.008	0.041 ± 0.003	≤0.008	...

NOTES.—Upper limits are 3 σ values. Uncertainties listed are due to continuum placement and do not include the flux calibration uncertainty of about 30%–50%. Fluxes are in units of 10^{-14} ergs cm^{-2} s^{-1} .

instrumental and sky background noise, and an additive constant was applied to null the signal on portions of the chip receiving no light. Most of the observed sources were sufficiently compact that we were able to maximize our observing efficiency by beam switching along the slit, keeping the source on the detector at all times. Spectra for the two source positions along the slit (or “on-source” and “off-source” for the more extended objects) were reduced separately and later combined to produce the final co-added spectrum.

Flat-field frames were obtained by imaging a flat surface illuminated by an internal incandescent lamp. The flats were normalized by a smoothed average frame before dividing them into the data. This self-normalization procedure removed large-scale features introduced by the optics, leaving the flat-field division to correct for small-scale pixel-to-pixel variations. We used the IRAF tasks *median* and *crmed* to remove bad pixels and cosmic rays when combining the individual object–sky pairs (typically 120 s frame $^{-1}$) accumulated for each source.

One-dimensional spectra were then extracted using the *apall* task in IRAF. The apertures were centered on the continuum peak for both stars and PNs, except for NGC 40 and BD +30 3639 (see details in § 3.4 and Table 1). For the compact PNs, the aperture width was generally set to be slightly larger than that of the strong Br γ line in order to include possible H $_2$ emission outside the ionized material (see Table 1; for objects with detected H $_2$ emission see § 3.4). Weak extended emission or a collimated outflow at an angle to our east-west slit would not have been detected. We compensated for atmospheric and instrumental effects by applying a spectral response curve, created by dividing a similarly reduced and smoothed spectrum of a nearby A, F, or G star (after interpolating across the stellar Br γ line) into a blackbody spectrum for that stellar temperature.

Stars with known near-infrared photometric fluxes were used for absolute flux calibration, and we measured the line fluxes with the line fitting package SPLLOT. Because of varying transparency and air mass, as well as variations in seeing and slit positioning and alignment, we estimate the uncertainty in absolute fluxes to be ~30%–50%. Thus, the nominal fluxes we present should be con-

sidered to be indicative only of general source brightness and may differ from other values in the literature, particularly for spatially extended objects for which our effective apertures may differ from those used by other authors. The quantities determined from relative spectrophotometry, namely, the line intensity ratios, are accurate to ~5%, except in regions of severe telluric absorption, such as near He I 2.058 μm (see § 3.1).

3. RESULTS

Our survey-mode spectral setup (Table 1) provides useful coverage from ~2.095 to 2.260 μm ; three of the targets were also observed with a second setup that extended farther to the blue (Table 2). Although our primary motivation was to study the H $_2$ emission, we also detected recombination and forbidden emission lines from the ionized gas. The measured line fluxes are summarized in Tables 3–5; where absolute fluxes are given, the units are 10^{-14} ergs cm^{-2} s^{-1} . Cited error bars include internal

TABLE 4
LINE FLUXES FOR IC 5117, M 1-13, AND Vy 2-2

λ	ID	IC 5117	M 1-13	Vy 2-2
2.033 μm	H $_2$ 1–0 S(2)	3.4 ± 0.7	2.6 ± 0.1	≤0.6
2.058 μm	He I	33.6 ± 0.2	1.7 ± 0.1	58 ± 4
2.073 μm	H $_2$ 2–1 S(3)	1.0 ± 0.3	≤0.3	≤0.4
2.113 μm	He I	8.7 ± 0.5	≤0.2	4.5 ± 0.2
2.122 μm	H $_2$ 1–0 S(1)	12.5 ± 0.2	6.0 ± 0.2	2.1 ± 0.2
2.145 μm	[Fe III]	≤1.2	≤0.2	0.44 ± 0.10
2.154 μm	H $_2$ 2–1 S(2)	≤1.4	≤0.2	≤0.5
2.166 μm	H I Br γ	95 ± 0.5	3.6 ± 0.1	65 ± 3
2.189 μm	He II	3.7 ± 0.2	≤0.2	≤0.5
2.199 μm	[Kr III]	2.5 ± 0.4	≤0.2	≤0.4
2.201 μm	H $_2$ 3–2 S(3)	≤1.2	≤0.2	≤0.4
2.218 μm	[Fe III]	≤1.1	≤0.2	1.3 ± 0.2
2.223 μm	H $_2$ 1–0 S(0)	3.4 ± 0.1	1.2 ± 0.1	0.85 ± 0.20
2.243 μm	[Fe III]	≤1.1	≤0.2	0.6 ± 0.1
2.247 μm	H $_2$ 2–1 S(1)	2.1 ± 0.4	0.78 ± 0.25	≤0.3

NOTE.—All fluxes are in units of 10^{-14} ergs cm^{-2} s^{-1} .

TABLE 5
LINE FLUXES FOR BD +30 3639, NGC 40, AND SwSt 1

λ	ID	BD +30 3639	NGC 40 West	SwSt 1
2.113 μm	He I	0.8 ± 0.2	≤ 0.30	8.2 ± 0.8
2.122 μm	H ₂ 1-0 S(1)	6.9 ± 0.2	0.71 ± 0.13	12.0 ± 0.6
2.145 μm	[Fe III]	≤ 0.5	≤ 0.30	3.3 ± 1.0
2.154 μm	H ₂ 2-1 S(2)	≤ 0.5	≤ 0.30	≤ 1.0
2.166 μm	H I Br γ	9.5 ± 0.5	12.2 ± 0.3	210 ± 5
2.189 μm	He II	≤ 0.5	≤ 0.20	≤ 1.5
2.199 μm	[Kr III]	≤ 0.4	1.20 ± 0.10	1.6 ± 0.6
2.201 μm	H ₂ 3-2 S(3)	0.9 ± 0.2	≤ 0.25	≤ 1.5
2.218 μm	[Fe III]	≤ 0.4	≤ 0.25	6.5 ± 1.0
2.223 μm	H ₂ 1-0 S(0)	2.2 ± 0.2	0.28 ± 0.10	3.8 ± 0.8
2.243 μm	[Fe III]	≤ 0.4	≤ 0.30	2.2 ± 0.5
2.247 μm	H ₂ 2-1 S(1)	1.9 ± 0.2	≤ 0.30	≤ 1.5

NOTE.—All fluxes are in units of 10^{-14} ergs cm^{-2} s^{-1} .

uncertainties only (those due to fitting line profiles and determining the continuum level) and do not include the overall scaling uncertainty in the absolute fluxes. The upper limits listed in Tables 3–5 are 3σ values based on these internal uncertainties.

Table 3 provides an overview of the main features seen in the full sample, including the brightest lines (in this spectral region) of both ionized and molecular species. Six of the sources show two or more lines of H₂, as well as lines of [Kr III] and [Fe III] as noted in column (6). The spectra of these 6 PNs are displayed in

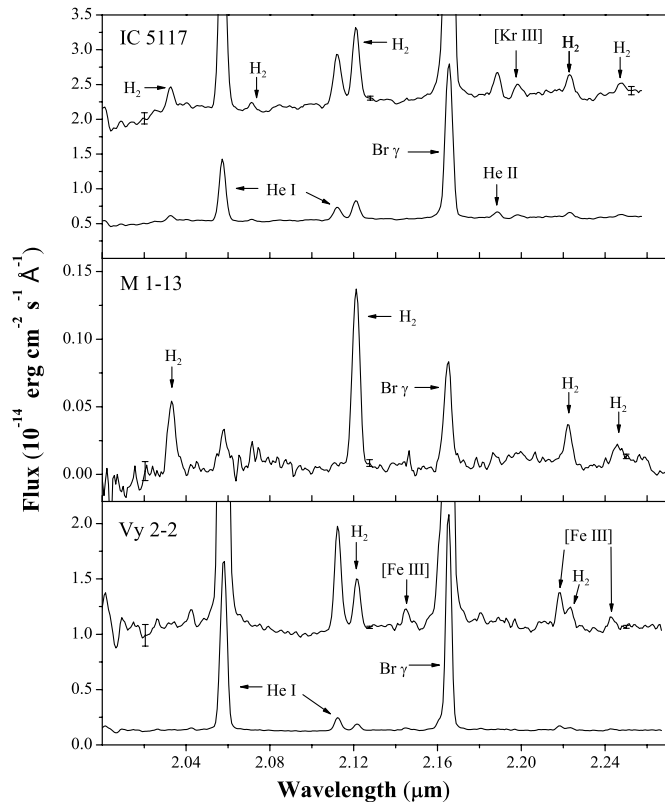


FIG. 1.—K-band spectra of IC 5117, M 1-13, and Vy 2-2. These are composites of the primary and supplementary wavelength setups described in the text and specified in Tables 1 and 2. For IC 5117 we show both the spectrum auto-scaled to Br γ (lower curve) and a second trace, expanded vertically by a factor of 4 in order to show details for the weaker lines (upper curve); for Vy 2-2, the upper curve is expanded by a factor of 8. IC 5117 shows a marginal detection of the 2.073 μm H₂ line, which peaks in the data at 2.071 μm . The major spectral features discussed in the text are identified in one or more of the panels.

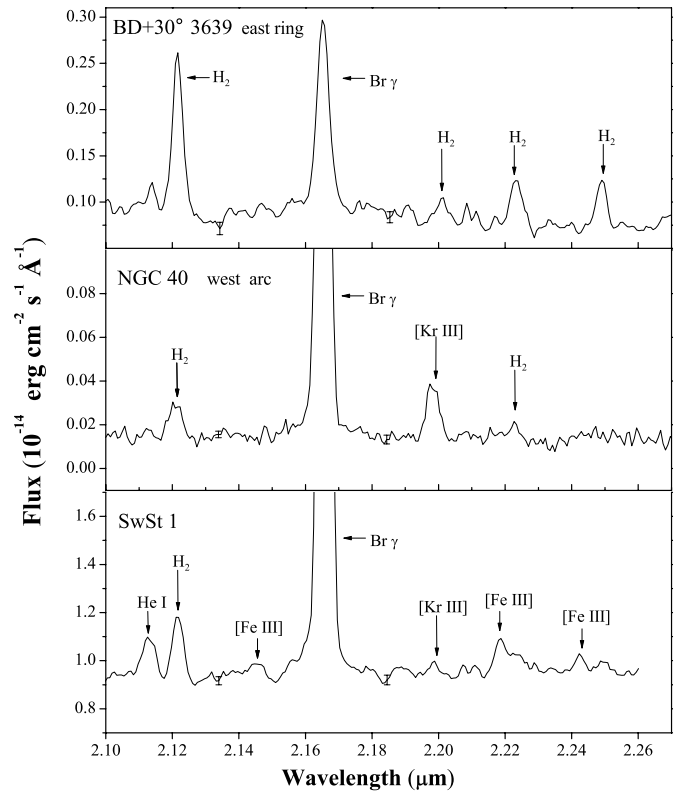


FIG. 2.—K-band spectra of BD +30 3639, NGC 40, and SwSt 1. These sources were observed in only one wavelength setup (the primary setting) and therefore have slightly more restricted spectral coverage than the objects shown in Fig. 1. The major spectral features discussed in the text are identified in one or more of the panels.

Figures 1 and 2, and a complete listing of their line intensities is given in Tables 4 and 5, respectively. In Table 3 we list the measured Br γ fluxes in absolute flux units, while the strengths of the other lines are given as ratios to Br γ . Tables 4 and 5 present all the line fluxes in absolute units. Preliminary reports on the overall project and some individual objects (specifically, IC 5117 and M 1-13) were previously presented by Likkel et al. (2000a, 2000b, 2002, 2004).

The continuum in this spectral region is composed of contributions from (1) the central star, in cases in which it is bright and included in the extraction aperture; (2) bound-free and free-free emission from the ionized gas, particularly for compact, high surface brightness sources; and (3) thermal emission from hot dust. Given the short wavelengths of these observations, the dust contribution likely arises from small grains that undergo excursions in temperature due to their small heat capacities, the process of “nonequilibrium” heating seen in reflection nebulae and throughout the diffuse interstellar medium (ISM; e.g., Sellgren et al. 1983; Draine 2004). We do not attempt to decompose the continuum into these constituents, since we are primarily concerned here with the emission lines.

3.1. H and He Recombination Lines

For all of the observed PNs except M 1-13, the strongest line is H I Br γ 2.166 μm . Its flux is given in column (2) of Table 3, while columns (3)–(5) summarize the strengths of the main H₂, He I, and He II lines in this spectral region. There are no other comparably strong H I lines in this portion of the K band. Br δ 1.945 μm lies just shortward of our coverage, near the edge of the photometric window, while the weak high-order members of the Pfund series fall at $\lambda \geq 2.35$ μm . In general, our Br γ fluxes are in reasonable

agreement with previously published values, given uncertainties in absolute flux calibration and differences in effective apertures (see § 2).

The He II line at $2.189\ \mu\text{m}$ is seen in seven of our targets, having the greatest strength in the high-excitation PN IC 2003, where it reaches almost 25% the strength of Br γ . This is similar to the highest values found by Lumsden et al. (2001b), who intentionally selected a sample of PNs covering a wide range of central star effective temperatures. The lowest values we find are $F_{2.189\ \mu\text{m}}/F_{\text{Br}\gamma} \leq 1\% - 2\%$. Since photon energies $>54\ \text{eV}$ are required to produce He $^{++}$, detectable He II recombination lines require fairly high central star temperatures ($T_{\text{eff}} \geq 50,000 - 60,000\ \text{K}$). In general, the strengths of He II lines, for example, the most commonly observed optical transition at $4686\ \text{\AA}$, increase with higher stellar temperature, but the strength of the $2.189\ \mu\text{m}$ line also depends on other factors, such as nebular optical depth effects (Kaler & Jacoby 1989; Köppen & Priete-Martinez 1991; Gruenwald & Viegas 2000). For nonobscured sources like the PNs in our study, there is no particular advantage in using He II $2.189\ \mu\text{m}$ rather than optical data, in which a wider variety of lines is available.

We detect the He I blend at $2.113\ \mu\text{m}$, which consists of two lines at 2.1120 and $2.1132\ \mu\text{m}$, in all but four of the observed PNs, including every object for which we detect He II $2.189\ \mu\text{m}$ except Me 2-1 and J900. The observed fluxes range from $\sim 2\%$ to 9% of the strength of Br γ . In five relatively high excitation targets, IC 2003, IC 2165, J900, Me 2-1, and Vy 2-2, the $2.113\ \mu\text{m}$ blend is weaker than He II $2.189\ \mu\text{m}$. The weakest He I $2.113\ \mu\text{m}$ lines are seen in some of the PNs with the coolest central stars, e.g., Cn 3-1 and SwSt 1. (For NGC 40 and M 1-13, which were observed at off-center positions where Br γ itself is weak, we measure only upper limits.) The strength of the $2.113\ \mu\text{m}$ line depends on several other effects in addition to central star temperature, including modest ($\sim 30\%$) variations due to enhancements in the elemental He abundance caused by the convective dredge-up of processed material and collisional and optical-depth effects (Lumsden et al. 2001b, their § 5.3).

The strongest He I line in the *K* band is at $2.058\ \mu\text{m}$, but our wavelength coverage includes this feature for only three targets (see Tables 2 and 4). We find that its flux relative to Br γ is ~ 0.35 , 0.5 , and 0.9 in IC 5117, M 1-13, and Vy 2-2, respectively, well within the range of values found by previous authors (e.g., DePoy & Shields 1994). In view of the ease with which this pair of lines can be measured in faint and/or obscured sources, there has been considerable interest in using it as an indicator of central star temperature for PNs (and other nebulae). Unfortunately, the strength of the He I $2.058\ \mu\text{m}$ line is even more severely affected by radiative transfer effects than is the $2.113\ \mu\text{m}$ He I blend, since it arises from a level that is resonantly pumped by $584\ \text{\AA}$ photons (DePoy & Shields 1994; Lumsden et al. 2001b). It also suffers from interference by strong, usually spectrally unresolved, telluric absorption due to CO $_2$. We therefore do not attempt to use this line to infer properties of these well-studied central stars or nebulae.

Several other He I lines nominally fall within in our spectral region, in particular $2.165\ \mu\text{m}$, which Lumsden et al. (2001b) recommend as an indicator of stellar temperature. However, this line is substantially weaker than the others discussed above, and it lies too close to the wing of the strong H I Br γ line for us to spectrally resolve with our instrumental setup.

3.2. H $_2$ Emission

3.2.1. Detection Rate for H $_2$ $2.122\ \mu\text{m}$

As can be seen from Table 3, half of our targets (8/16) show H $_2$ $v = 1-0\ S(1)\ 2.122\ \mu\text{m}$ emission at flux levels greater than our

detection limit. This should not, however, be interpreted as indicating that 50% of all PNs show H $_2$ emission, because this is not an unbiased sample; indeed, it is not clear whether any studies to date have been done on a truly unbiased sample. In fact, we specifically selected several targets that exhibited indicators of neutral or molecular material such as H I $21\ \text{cm}$ or CO millimeter line emission, or Na I absorption (see Table 5 of Dinerstein et al. 1995), or that were known from prior spectroscopic or imaging work to show H $_2$ $2.122\ \mu\text{m}$ emission (Kastner et al. 1996; HLD99). We report the first H $_2$ line ratios for M 1-13 and SwSt 1, also detecting two or more H $_2$ emission lines from NGC 40, Vy 2-2, BD +30 3639, and IC 5117. For IC 2003 and J900 we have $\geq 3\ \sigma$ detections of only the $2.122\ \mu\text{m}$ H $_2$ line, and we did not detect any H $_2$ in Cn 3-1, IC 2165, IC 5217, M 1-4, M 1-6, Me 2-1, NGC 6210, or Vy 1-2.

Due to its intrinsic strength, the $2.122\ \mu\text{m}$ line is often used as a general tracer for the presence of H $_2$ in PNs. Imaging surveys have suffered from possible contamination of the nominal H $_2$ filter by He I $2.113\ \mu\text{m}$ (e.g., Kastner et al. 1996), except in the (rare) cases in which particularly narrow line filters that exclude the He I line are used (Latter et al. 1995). As discussed above, the intensity of $2.113\ \mu\text{m}$ relative to Br γ can vary with nebular properties other than the He $^+$ /H $^+$ abundance, making it nontrivial to correct the photometry for its contribution to the net emission in a broad filter passband. However, this problem is gradually being overcome by the growing availability of spectroscopic observations for a larger number of PNs (e.g., HLD99; LPH01; Guerrero et al. 2000; García-Hernández et al. 2002; Davis et al. 2003; this study).

Typically, studies that include a wide range of PN morphological types and stages of development (from PPNs to relatively evolved nebulae) detect H $_2$ emission in $\sim 30\% - 40\%$ of their targets (Kastner et al. 1996; García-Hernández et al. 2002). This is higher than the detection rate of the more fragile CO molecule, which is seen in $\sim 20\%$ of surveyed PNs (Huggins et al. 1996). On the other hand, surveys that focus on bipolar PNs (e.g., Kastner et al. 1994) tend to find much higher detection rates, in some cases approaching 100% (Guerrero et al. 2000)! Thus, the incidence rate of 50% that we find is quite consistent with detection rates for other studies of samples chosen with similar selection criteria.

3.2.2. Other *K*-Band H $_2$ Lines

We detect multiple H $_2$ lines in six sources (Tables 4 and 5). In the limited spectral region we cover, the next strongest H $_2$ line after $1-0\ S(1)\ 2.122\ \mu\text{m}$ is generally $1-0\ S(0)\ 2.223\ \mu\text{m}$; the comparably strong $1-0\ S(2)\ 2.033\ \mu\text{m}$ line was included for only three targets. The typical intensity ratio ($F_{2.223}/F_{2.122}$) is about $\frac{1}{3}$. The other H $_2$ lines in our spectral range arise from higher vibrational states, $v' = 2$ and 3 , and are generally weaker than 20% of $2.122\ \mu\text{m}$. We detect H $_2\ 2-1\ S(1)\ 2.247\ \mu\text{m}$ in three PNs and $3-2\ S(3)\ 2.201\ \mu\text{m}$ probably only in BD +30 3639. In § 4 we summarize the observed line ratios, compare them to predictions for PDRs and shock excitation, and discuss the implications for understanding the excitation mechanism of H $_2$ in PNs.

3.2.3. Spatial Distribution of the H $_2$ Emission

The ionization front and PDR in a planetary nebula will move outward as the nebula evolves, so one might expect that molecular emission will extend further from the central star than tracers of the ionized gas. In this case, the object's apparent size when imaged in emission from the PDR may be larger than its size in a transition from the ionized zone (e.g., Graham et al. 1993b; Latter et al. 2000). On the other hand, if the molecules are primarily located in small, dense clumps embedded within the

ionized region, the vibrationally excited H_2 will be located at the edges of the clumps and possibly contained within the main body of the nebula (Huggins et al. 2002; Speck et al. 2003; O'Dell et al. 2005). If the clumps in our more distant sample have linear sizes similar to the clumps seen in nearby, well-resolved PNs (e.g., Speck et al. 2002; O'Dell et al. 2002), we would not be able to distinguish between the distributions of the ionized and molecular emission.

For M 1-13, which we resolve reasonably well, our long-slit (see § 2) spectroscopic data show that the H_2 line clearly extends beyond the $Br\gamma$ emission. However, for all seven other PNs in which we detected H_2 , its spatial extent appears similar to that of $Br\gamma$. On the other hand, this could be simply a threshold effect given that our ability to measure the extent of an emission component is highly dependent on the line strength, and in all the PNs we observed, $Br\gamma$ is much brighter than the H_2 line, except for M 1-13. Thus, in the other sources we are able to trace the $Br\gamma$ emission down to a small fraction of its peak surface brightness, while in H_2 we see only the brightest regions. For example, although we cannot conclusively distinguish between the sizes of the H_2 - and $Br\gamma$ -emitting regions in BD +30 3639 with our data, observations of this PN with higher spatial resolution and sensitivity have confirmed that the H_2 emission does in fact extend beyond the ionized region (e.g., Shupe et al. 1998).

3.3. Ionized Lines of Heavy Elements: Fe and Kr

3.3.1. [Kr III] 2.199 μm and the Krypton Abundance

Two unidentified emission lines at 2.199 and 2.287 μm were discovered in the early K -band spectroscopic observations of NGC 7027, which also yielded some of the first detections of H_2 emission in a PN (Treffers et al. 1976; Smith et al. 1981). The unidentified transitions were addressed by Geballe et al. (1991), who pointed out that despite their close proximity to lines of H_2 , they must arise from some other species, one residing in the ionized region. More recently, Dinerstein (2001) finally identified these lines as fine-structure transitions from ions of transiron elements that can be self-enriched in asymptotic giant branch (AGB) stars and in their descendants, PNs, by the s -process, slow neutron captures onto iron seed nuclei. In particular, 2.199 μm is the $^3P_1 - ^3P_2$ [Kr III] line, and the 2.287 μm line is [Se IV] $^2P_{3/2} - ^2P_{1/2}$. The latter lies outside our spectral coverage, but we detected [Kr III] in IC 5117, SwSt 1 (a marginal detection), and both extracted positions for NGC 40.

Since these lines arise from species made by neutron-capture reactions in the progenitor AGB stars, they offer an opportunity to measure nucleosynthetic yields for these elements in PNs, a significant conduit of recycled and chemically altered material to the ISM (Busso et al. 1999). The K -band lines are readily detectable in many PNs, which makes them particularly suitable for a survey to assess the fraction of PNs that show enhanced abundances of these s -process products and to determine enrichment factors (Dinerstein 2004b). Such a survey is being conducted at McDonald Observatory with the same instrument used for this study. Preliminary results have been reported by Sterling & Dinerstein (2004, 2005a, 2005b), and a detailed analysis including use of photoionization models to make corrections for other ionic stages will be carried out as part of the Ph.D. dissertation of N. C. Sterling (2006, in preparation). Results to date indicate that the abundances of these elements in PNs range from roughly solar (i.e., no enhancement) up to enrichment factors of ~ 5 –10 times solar (Sterling & Dinerstein 2004). This is similar to the range of enrichment factors found for Ge, another light n -capture element (Sterling et al. 2002, 2005).

We use the flux ratio of [Kr III] 2.199 μm to $Br\gamma$ (and the ratio of the emissivities of these lines) to infer the ionic abundance ratio $n(\text{Kr}^{++})/n(\text{H}^+)$, as in Dinerstein (2001). This is a lower limit for the elemental ratio $n(\text{Kr})/n(\text{H})$, since Kr may also be present in other ionic states; for example, there may be a significant fraction of Kr present in Kr^+ for the low-excitation objects SwSt 1 and NGC 40. We neglect correction of the observed line ratio for reddening, which is negligible because of the small wavelength separation of the lines, low extinction in the K band, and small total extinction toward these objects. The emissivity of the [Kr III] 2.199 μm line is given by $\epsilon_{2.199} = (A_{21}h\nu f_2)/n_e$, where f_2 is the fraction of Kr^{++} ions in the upper level of the transition. While this fractional population is a function of T_e and n_e , in this regime $f_2 \propto n_e$, so that the line emissivity is insensitive to density (the critical density, at which the collisional de-excitation rate balances the radiative transition rate, is $2.1 \times 10^7 \text{ cm}^{-3}$). In addition, $\epsilon_{Br\gamma}$ is nearly independent of n_e , while varying approximately as $T_e^{-1.1}$. For each PN in which we detect [Kr III], we take T_e and n_e values from the literature and interpolate the $Br\gamma$ emissivity for these parameters, assuming case B recombination from Tables B.5 and B.9 of Dopita & Sutherland (2003). Where Dinerstein (2001) used an analytic three-level approximation to solve for f_2 , here we calculate it as a function of T_e and n_e from a five-level atom equilibrium solution (Sterling & Dinerstein 2005b), using the collision strengths of Schöning (1997) and transition probabilities from Biémont & Hansen (1986).

For IC 5117, Dinerstein (2001) previously derived $n(\text{Kr}^{++})/n(\text{H}^+) = 3.3 \times 10^{-9}$, about 60% higher than solar. We have revised the absolute flux calibration for this data, which lowers the absolute line fluxes of both [Kr III] 2.199 μm and $Br\gamma$ but leaves the ratio of line intensities essentially unchanged: 0.026 ± 0.004 compared to our earlier value of ~ 0.030 . (Note that Rudy et al. [2001] find a flux ratio of 0.016 ± 0.005 .) We assume $T_e = 12,000 \text{ K}$ and $n_e = 10^5 \text{ cm}^{-3}$ (Hyung et al. 2001), for which $\epsilon_{Br\gamma} = (4\pi j)/(n_e n_p) = 2.76 \times 10^{-27} \text{ ergs cm}^3 \text{ s}^{-1}$ and $\epsilon_{2.199 \mu\text{m}} = 3.38 \times 10^{-20} \text{ ergs cm}^3 \text{ s}^{-1}$. This yields $n(\text{Kr}^{++})/n(\text{H}^+) = 2.1 \times 10^{-9}$, consistent with the solar value of $(1.9 \pm 0.3) \times 10^{-9}$ (Asplund et al. 2005). However, IC 5117 is a fairly high excitation PN in which there is over 10 times more oxygen in O^{++} than in O^+ (Hyung et al. 2001; Pottasch et al. 2003). If the ionic fractions are similar, i.e., $n(\text{Kr}^{++})/n(\text{Kr}) \approx n(\text{O}^{++})/n(\text{O})$, in parallel with the similar ionization potentials of Kr III and O II, the total krypton abundance could be an order of magnitude larger than the abundance of Kr^{++} . However, this assumption about the ionization balance is an oversimplification; the ionization equilibrium of Kr in IC 5117 and a number of other PNs will be examined via detailed photoionization modeling by N. C. Sterling et al. (2006, in preparation).

The other two PNs in which we detected [Kr III] have considerably lower nebular excitation, so that most of the Kr probably resides in this ion. For SwSt 1 we have line emissivities of 3.40×10^{-27} and 3.36×10^{-20} , respectively, for $Br\gamma$ and [Kr III] at $T_e = 10,000 \text{ K}$ and $n_e = 3 \times 10^4$ (De Marco et al. 2001; Sterling et al. 2005). For the observed line fluxes (Table 5), we find $n(\text{Kr}^{++})/n(\text{H}^+) = (0.8 \pm 0.2) \times 10^{-9}$, but note that the line flux is very uncertain. Although they do not quote a value for it, the [Kr III] line is also visible in the near-infrared spectrum of SwSt 1 presented in Appendix B of De Marco et al. (2001), with a flux ratio about twice our value (O. De Marco 2003, private communication). This is discussed further in § 3.4.4.

Finally, in NGC 40 we have the clearest case of an overabundance of Kr. In the aperture centered on the western arc, we measure $F_{2.199 \mu\text{m}}/F_{Br\gamma} = 0.098 \pm 0.010$, and we use $T_e = 8000 \text{ K}$ and $n_e = 3000 \text{ cm}^{-3}$ (Meaburn et al. 1996; Sabbadin et al. 2000), for which

$\epsilon_{\text{Br}\gamma} = 4.38 \times 10^{-27}$ ergs cm³ s⁻¹ and $\epsilon_{2.199 \mu\text{m}} = 3.19 \times 10^{-20}$ ergs cm³ s⁻¹. This yields $n(\text{Kr}^{++})/n(\text{H}^+) = (13.5 \pm 1.4) \times 10^{-9}$, which corresponds to 7 ± 2 times the solar abundance of Kr in the form of Kr^{++} alone. Given the low excitation of this PN (see § 3.4.1), the correction for higher ionization stages of Kr is likely to be modest, but there might be some Kr^+ , which we do not observe. Therefore, we conclude that $n(\text{Kr})/n(\text{H}) \gtrsim 7$ times solar in NGC 40, a very significant enhancement. It is interesting that NGC 40 has a Wolf-Rayet ([WC])–type central star, in view of the fact that we find that PNs with this type of central star tend to have greater enrichments in *s*-process products (Sterling et al. 2002; Sterling & Dinerstein 2005a, 2005b).

3.3.2. [Fe III] Lines

In two PNs, SwSt 1 and Vy 2-2, we detect three [Fe III] lines from the multiplet connecting the ³G and ³H terms, at 2.145, 2.218, and 2.243 μm (Tables 4 and 5). These comprise three of the four strongest (magnetic dipole) transitions of this multiplet in the *K* band (Garstang 1957; Nahar & Pradhan 1996; Quinet 1996); the fourth, at 2.348 μm , lies outside our spectral range. DePoy & Pogge (1994) measured these lines in the Orion H II region, calling attention to the presence of spatial positions where the [Fe III] lines are unusually strong relative to Br γ . They highlighted the potential danger of blending or confusing the [Fe III] lines with nearby H₂ transitions, leading to misinterpretation of the H₂ emission. In particular, they point out that the [Fe III] 2.218 μm line can be blended with or misidentified as 1–0 *S*(0) H₂ 2.223 μm , and [Fe III] 2.243 μm can be similarly confused with 2–1 *S*(1) H₂ 2.247 μm . This is a significant issue because the ratios of these two lines to 1–0 *S*(1) 2.122 μm have been widely used to identify the excitation mechanism of the near-infrared H₂ lines. While this caveat is raised by DePoy & Pogge (1994) in the context of H II regions, we find here that it also applies to PNs.

The near-infrared [Fe III] multiplet, despite its long wavelengths and low photon energies, actually arises from high-excitation energy levels (in contrast to [Kr III] 2.199 μm , which comes from the first excited fine-structure level above ground). Indeed, the originating energy levels actually lie *above* the levels that give rise to the optical [Fe III] lines at ~ 4000 –5400 Å (e.g., see Fig. 6 of Bautista & Pradhan 1998, hereafter BP98). For example, the brightest line of the near-infrared multiplet ³G₅–³H₆ 2.218 μm arises from a level that lies 24,558.8 cm⁻¹ above the ground state (Ekberg 1993), which corresponds to 35,400 K. Consequently, the strengths of the lines of this multiplet are quite sensitive to *T_e* (e.g., Keenan et al. 1992, hereafter K92; BP98) although the line ratios are not (see § 5). These lines can also be strong if the ionic abundance $n(\text{Fe}^{++})/n(\text{H}^+)$ is high, either because a large fraction of the elemental Fe is in the gas phase rather than in the dust grains, or because of a higher elemental abundance. Charge exchange can reduce the [Fe III] line strengths from regions where neutral hydrogen atoms are present by converting Fe⁺⁺ to Fe⁺. Variations in [Fe III] line strengths have been seen to be very localized (Luhman et al. [1998] and DePoy & Pogge [1994] in the Orion region; Lutz et al. [1993] in the Galactic center). Indeed, substantial variations in the gas-phase abundance of Fe⁺⁺ along different lines of sight within SwSt 1 itself were noted by Sterling et al. (2005), who interpret it in terms of different degrees of elemental iron depletion into dust.

In addition to our detections in SwSt 1 and Vy 2-2, we marginally detect [Fe III] 2.218 μm in Cn 3-1. Optical [Fe III] lines have been measured in all three objects (K92 and references therein; Perinotto et al. 1999; De Marco et al. 2001), but there are no previous explicit reports of near-infrared [Fe III] lines in these objects. Of the 39 PNs they surveyed, the only object for which

HLD99 detected [Fe III] 2.218 μm was Vy 2-2, for which they list an unidentified line at 2.2184 μm (see their Table 6). The [Fe III] lines are also present in the near-infrared spectrum of SwSt 1 (O. De Marco 2003, private communication), although they are not easily seen in Figure B2 of De Marco et al. (2001), in which the vertical scale is optimized to show the brighter lines. A few other detections of the *K*-band [Fe III] lines appear in the literature, generally in very bright sources or very deep spectra (e.g., Luhman & Rieke 1996), but are rare compared to detections of infrared [Fe II] lines, which are particularly prominent in the *J* and *H* bands. The strengths and ratios of the near-infrared [Fe III] emission lines in PNs, their use as diagnostics of physical conditions (in particular *n_e*), and implications for dust formation and destruction are discussed in § 5.

3.4. Notes on Individual Objects

3.4.1. NGC 40

NGC 40 is one of the most extended PNs in our sample. The morphology of the main shell is a broken ellipse with the major axis tilted slightly east of north, and the highest surface brightness contours are located in two narrow arcs about 8''5 east and west of the central star (e.g., Jacoby et al. 1987). Deeper exposures reveal fainter loops and jets “breaking out” along the poles of the major axis, and the velocity field is turbulent and complex (Meaburn et al. 1996; Sabbadin et al. 2000). For our observations we placed an east-west slit 7''4 north of the central star. In this position, the slit passed through both east and west arcs, and we extracted spectra centered on both (see Table 1). Unfortunately, we were forced to discard about a third of the integrations, for which poor cancellation of night sky lines indicated variable observing conditions (see Table 1).

The Br γ line dominates the *K*-band spectrum of NGC 40. It is strong in both arcs and is also seen faintly along the entire portion of the slit between the arcs. The west arc, which was also observed by HLD99, is more than twice as bright (in Br γ) as the east position. Our spectrum of the west arc (Fig. 2, *middle*) also shows [Kr III] 2.199 μm and two H₂ transitions, while the east arc shows only [Kr III] and Br γ . The ratio of [Kr III] to Br γ is the same in both arcs within measurement uncertainties, $\approx 0.10 \pm 0.01$, and agrees with the value of HLD99, who label the 2.199 μm line as UID 1 after Geballe et al. (1991). In § 3.3.1 we showed that this flux ratio implies a large enhancement in the ionic and elemental abundance of Kr, presumed to be due to convective mixing of *s*-processed material from the stellar interior during the AGB phase.

Our value for the ratio $F(\text{H}_2 \text{ 2.122 } \mu\text{m})/F(\text{Br}\gamma) \approx 0.06$ is consistent with that found by HLD99. We find $F(\text{H}_2 \text{ 2.223 } \mu\text{m})/F(\text{H}_2 \text{ 2.122 } \mu\text{m}) \approx 0.4 \pm 0.2$. This is a plausible value for the line ratio but is not particularly helpful in distinguishing between different possible H₂ excitation mechanisms (§ 4). HLD99 did not report seeing the 2.223 μm line but did detect strong *Q*-branch lines from *v* = 1 levels. Apparently the H₂ emission is too weak, or perhaps too spatially similar to that of the ionized gas, to have been noticed in imaging surveys, which have classified NGC 40 as a PN without near-infrared H₂ emission (Latter et al. 1995; Kastner et al. 1996).

3.4.2. J900

J900 is a fairly high excitation PN, as indicated by our detection of [He II] 2.189 μm but not [He I] 2.113 μm (Table 3). The optical morphology is a compact bipolar structure with lobes separated by about 3''5. J900 was originally assigned to the class of H₂-emitting PNs based on narrowband images that showed a

distinctly different morphology in “H₂” filters than in bands tracing the ionized gas (Latter et al. 1995, Figs. 12 and 19). The most in-depth imaging of the H₂ emission was performed by Shupe et al. (1995), who delineated jets emerging from the bipolar axis and extending well beyond the ionized core, as well as fainter H₂-emitting clumps at larger angular distances. For our observations, we rotated the slit to a position angle 130° east of north in order to align with the nebula’s major axis and include both bright inner lobes seen in H₂ 2.122 μm (Shupe et al. 1995, Figs. 2a and 3).

Near-infrared spectroscopic observations of J900 were reported by HLD99, who list fluxes for several H₂ lines, of which only the $v = 1-0$ S(1), S(2), S(3), and Q(1-3) lines were detected with significance levels of 2.5 σ or higher. We detect only three spectral lines, Br γ , He II, and H₂ 2.122 μm , with confidence. (The [Kr III] line was detected in subsequent observations and will be reported by N. C. Sterling et al. [2006, in preparation].) Our observing aperture must have included a larger contribution from the ionized gas than that of HLD99, who do not detect Br γ at their position north of the nebula’s major axis, northwest of the central star. The fact that we do not detect any H₂ lines other than 2.122 μm is probably a consequence of the faintness of the source, which places these weaker transitions below our detection limit. Shupe et al. (1995) argue on purely morphological grounds that the H₂ is shock excited, but this argument may not be conclusive, since the observed structures (narrow jets and limb-brightened cones) could also result from nonuniform illumination by the central UV source (e.g., through polar holes in an optically thick torus). Without knowing the excitation mechanism it is difficult to estimate a molecular mass from H₂ emission. Huggins et al. (1996) detect CO 2-1 but not CO 1-0 emission and derive a rather small corresponding molecular mass, $4 \times 10^{-4} M_{\odot}$, one of the lowest values in their table of 44 PNs detected in CO.

3.4.3. M 1-13

M 1-13 is another fairly large, bipolar PN, with an optical diameter of 27'' (Corradi & Schwarz 1995; Kastner et al. 1996; Górný et al. 1999). Interestingly, the H₂ image of Kastner et al. (1996) bears a noticeable resemblance to the optical image of NGC 40, with narrow arcs enclosing a roughly elliptical core and polar elongations protruding beyond the extrapolated elliptical contour. The waist of the nebula, where Kastner et al. find the strongest H₂ emission, is tilted by $\sim 20^\circ$ from east-west (P.A. 160°; cf. Kastner et al. 1996) but is wide enough that our east-west slit fell fully within it. The 1''8 slit was centered on the nebula and the spectra extracted from an 18'' aperture.

A glance at our spectrum of M 1-13 (Fig. 1, *middle*) demonstrates that this PN deserves to be designated as “H₂-dominated,” in the nomenclature of HLD99. The H₂ 2.122 μm line is stronger than all of the H and He recombination lines, including Br γ , which is only 60% the strength of H₂ 2.122 μm . Also easily detected are H₂ 2.033, 2.223, and 2.248 μm . We see 2.122 μm emission all along the waist (with a linear extent of 12''6), but it is strongest at the rims, suggesting that the H₂ arises from a limb-brightened ring. The Br γ emission is less extended (10''8) along our slit than the H₂. Our upper limit on He I 2.113 μm ($\leq 0.1 \times \text{H}_2$ 2.122 μm) confirms that the image by Kastner et al. (1996) of this source was not contaminated by He I, and therefore gives a good representation of the spatial distribution of the H₂ emission in this source.

The strong H₂ emission from M 1-13 indicates the presence of a large amount of molecular material, efficient excitation of H₂, or both. As is discussed in § 4, the observed H₂ line ratios suggest that thermal excitation, which generally results in higher surface

brightness emission, dominates. On the other hand, there is other evidence for substantial amounts of molecular material; Huggins et al. (1996) see both the CO 1-0 and 2-1 lines in M 1-13 and compute an equivalent molecular mass of $\sim 0.18 M_{\odot}$.

3.4.4. SwSt 1

SwSt 1 is a compact, young, and dense PN (Kwok et al. 1981; Flower et al. 1984), with a hydrogen-deficient Wolf-Rayet central star (HD 167362). A recent detailed study of the star and nebula shows that the nebula is O-rich, even though the stellar photosphere is C-rich with extreme abundance ratios characteristic of material that has undergone substantial nuclear processing and convective dredge-up (De Marco et al. 2001). De Marco et al. (2001) present *Hubble Space Telescope* (HST) images taken in emission lines from the ionized gas, showing a clumpy ring of an approximate extent $1''.3 \times 0''.9$. These dimensions are consistent with previous estimates, radio continuum sizes of 1'' and 1''.3 were reported by Kwok et al. (1981) and Aaquist & Kwok (1990), respectively. Using a diameter of 1''.3 and the nebular expansion velocity, De Marco et al. (2001) infer a dynamical age of only ≈ 300 yr. However, we determined a larger size than previously reported (discussed below).

Our *K*-band spectrum of SwSt 1 (Fig. 2, *bottom*) is dominated by the H I and He I lines, but we also detect two H₂ lines, 1-0 S(1) 2.122 μm and 1-0 S(0) 2.223 μm . We initially suspected that two lines of the $v = 2-1$ series were also present (at 2.154 and 2.247 μm , respectively), but on closer inspection these features were found to actually be nearby [Fe III] lines (Table 5; § 3.3.2). The near-infrared spectrum of SwSt 1 shown in Appendix B of De Marco et al. (2001) also contains H₂, although they list a flux for only the 2.122 μm line. Their cited ratio of 2.122 μm to Br γ is consistent with our value (~ 0.05), and the ratio of H₂ 2.223 μm to 2.122 μm in their data, 0.30 (O. De Marco 2003, private communication), is consistent with ours (0.32 ± 0.08). The intensities of the other *K*-band lines in their spectrum are also consistent with our results within measurement uncertainties, the greatest difference being for [Kr III] 2.199 μm , which is essentially at our detection limit (§ 3.3.1).

Given our relatively large aperture and the poor seeing conditions at the time of our observations (the point-spread function [PSF] as estimated from a faint field star that fell within our slit was 2''.5–3''), we are not in a position to measure the angular size of the H₂-emitting region in SwSt 1 with high accuracy. However, our observations show an apparent angular extent along the slit (not deconvolved) of 4''.0–4''.5 for H₂ 2.122 μm , slightly larger than the similarly measured extent of the adjacent continuum, 3''.5. Interestingly, we can trace the Br γ line to a full east-west angular extent of at least 8'', with possible weak emission extending even farther. The fact that the ionized gas appears to have a larger diameter than the H₂ might be an artifact of the greater peak intensity of Br γ (see § 3.2.3). However, if the effect is real, it may instead be an indication that the H₂ emission arises from small clumps fully embedded within the ionized zone, as in the Ring Nebula (e.g., Speck et al. 2003). As discussed in § 4 (also Dinerstein 1991), the molecular mass corresponding to an observed H₂ line intensity depends on the emission mechanism. It is unlikely that the molecular mass in SwSt 1 is very large, in view of the fact that attempts to measure CO emission have yielded only upper limits. There is, however, evidence for neutral atomic material, from the detection of nebular Na I (Dinerstein et al. 1995) and H I 21 cm absorption projected against the radio continuum emission (Gussie & Taylor 1995; Huggins et al. 1996).

SwSt 1 stands out as being the only PN in our sample that shows both [Kr III] and [Fe III] emission (Table 3; § 3.3). In fact, it

TABLE 6
H₂ LINE FLUXES RELATIVE TO 1–0 S(1) 2.122 μ m

Model/PN ^a	log n (cm ⁻³)	log χ (\times ISRF)	$T_{1/2}$ (K)	1–0 S(2) 2.033	2–1 S(3) 2.074	2–1 S(2) 2.154	3–2 S(3) 2.201	1–0 S(0) 2.223	2–1 S(1) 2.247
(1)	(2)	(3)	(4)	(5)	(6)	(7)	(8)	(9)	(10)
BvD 14.....	3.5	3.0	100	0.50	0.35	0.28	0.18	0.47	0.56
A.....	4.0	4.0	200	0.42	0.44	0.24	0.24	0.37	0.58
B.....	4.5	4.0	300	0.39	0.46	0.21	0.23	0.33	0.51
D.....	5.0	4.0	500	0.32	0.16	0.07	0.07	0.29	0.18
F.....	5.0	5.0	550	0.31	0.14	0.06	0.06	0.28	0.15
H.....	5.5	4.5	650	0.31	0.08	0.03	0.02	0.28	0.09
S1.....	N/A	N/A	1000	0.27	<0.01	<0.01	<0.01	0.28	<0.01
S2.....	N/A	N/A	2000	0.37	0.08	0.03	<0.01	0.21	0.08
BD +30.....	≤ 0.07	0.10 ± 0.03	0.23 ± 0.05	0.20 ± 0.03
M 1-13.....	0.45 ± 0.04	≤ 0.07	≤ 0.05	≤ 0.03	0.21 ± 0.02	0.12 ± 0.04
IC 5117.....	0.27 ± 0.06	0.08 ± 0.03	≤ 0.11	≤ 0.10	0.28 ± 0.04	0.17 ± 0.03
Vy 2-2.....	≤ 0.29	≤ 0.19	≤ 0.24	≤ 0.19	0.40 ± 0.13	≤ 0.14
SwSt 1.....	≤ 0.08	≤ 0.12	0.32 ± 0.06	≤ 0.12
NGC 40W.....	≤ 0.42	≤ 0.35	0.39 ± 0.25	≤ 0.42

^a Models include the low-density radiatively excited model 14 of Black & van Dishoeck (1987), radiatively excited models at higher densities from B. Draine (2003, private communication), and line ratios for isothermal shocks at $T = 1000$ K (S1) and 2000 K (S2); $T_{1/2}$ is T_{kinetic} , where half the H is in H₂.

is a little surprising that the Kr abundance does not appear to be especially large (§ 3.3.1), since SwSt 1 shows evidence for a large enrichment in the neighboring element Ge, whose abundance is enhanced over solar by a factor of ≈ 5 , as indicated by *Far Ultraviolet Spectroscopic Explorer* (FUSE) observations of a resonance absorption line of Ge III (Sterling et al. 2005). On the other hand, the [Kr III] flux is uncertain, and no correction factor has been applied for other ions, so the abundances of Ge and Kr may still be consistent.

The strength of the [Fe III] lines in SwSt 1 may indicate an atypically high concentration of Fe in the gas phase, corresponding to a less extreme depletion into dust than, for example, in the cold ISM (§ 5). Whether this results from the incomplete condensation of refractory species into dust at the formation epoch (on the AGB) or postformation destruction of dust by some agent during the PN stage is unclear. What is clear, however, is that the depletion of Fe into dust along the restricted line of sight toward the central star of SwSt 1 is lower than in the line-emitting region, suggesting that the dust-to-gas ratio is inhomogeneous within the nebula (Sterling et al. 2005).

3.4.5. Vy 2-2

Vy 2-2, like SwSt 1 and IC 5117 (see below), is considered to be a “young” PN on the basis of the compact size ($\lesssim 0.3''$) and very high density of its ionized core (e.g., Seaquist & Davis 1983; Miranda & Solf 1991, hereafter MS91; Feibelman 1993; Christiano & Seaquist 1998). The central core shows barely resolved bipolarity on a subarcsecond scale (MS91; Sahai & Trauger 1998, Fig. 2d). Its dynamical age is only a few hundred years (MS91). Vy 2-2 was notable for being the first PN in which OH maser emission was ever detected (Seaquist & Davis 1983; Payne et al. 1988), and it has also been detected in CO (Huggins et al. 1996).

We find the angular diameter of the strong Br γ emission to be $8''.3$ (as for SwSt 1, this value is not corrected for deconvolution of the PSF), but we also see weaker emission extending to $11''$ east and $6''$ west of the continuum center. This is consistent with the structure seen in H α by MS91, who report a subarcsecond bright core surrounded by a halo of weak H α emission extending well beyond our Br γ extent. In comparison, we detect the (much weaker) H₂ 2.122 μ m line to only slightly beyond the $\sim 4''.3$

diameter continuum region. Possible reasons why our nominal H₂ “size” might be smaller than the extent of H I recombination emission are discussed above in the context of SwSt 1 (§ 3.4.4).

We attempted to optimize our ability to detect H₂ emission in the spectrum of Vy 2-2 by using an $8''.4$ extraction aperture that did not include all of the Br γ emission. However, we were able to securely detect only two H₂ lines, the $v = 1-0$ S(1) and S(0) lines (Fig. 1, bottom). Although our observed $F_{2.223}/F_{2.122}$ ratio suggests radiative excitation, our upper limit on the H₂ 2.247 μ m line is more consistent with shocks, unless the density is very high (Table 6). HLD99 also reported seeing H₂ in Vy 2-2, but only the S(1) and Q(1) lines were detected at $\geq 3\sigma$ significance. They also reported a marginally detected line at 2.2426 μ m, which they identified as $v = 2-1$ S(1) 2.247 μ m. However, we demonstrate here that it is actually [Fe III] 2.243 μ m. (As discussed in §§ 3.3.2 and 5, Vy 2-2 has particularly strong [Fe III] lines in both the optical and infrared, which may be partly a result of its very high density.) HLD99 tentatively reported a feature at 2.199 μ m (the [Kr III] line), with a strength that is excluded by our data.

3.4.6. BD +30 3639

BD +30 3639 is a well-studied, dense, young PN. Like NGC 40 and SwSt 1, its central star has a strong wind, is C-rich and H-deficient, and is classified as [WC] type. It was one of the first few PNs in which infrared H₂ emission was detected (Beckwith et al. 1978) and has been included in several near-infrared spectroscopic surveys (Geballe et al. 1991; HLD99; LPH01). In optical images it has the appearance of a slightly “squared-off” elliptical ($3''.5 \times 5''$) ring that is faintest along the western edge, clumpy on the smallest resolvable scales, and embedded in a somewhat larger envelope that may be primarily reflection nebulaosity (Harrington et al. 1997; Sahai & Trauger 1998).

According to previous studies, the H₂ emission lies primarily outside the ionized ring and is brightest along the eastern edge (Graham et al. 1993a; Shupe et al. 1998). We therefore centered our extraction aperture on the eastern H₂ lobe, placing the $10''.1$ wide aperture $8''.5$ east of the nebular center (see footnote to Table 1) in order to exclude the continuum from the bright central star and minimize the contribution from the ionized gas. As a consequence, our spectrum is dominated by H₂ lines, while lines from

the ionized gas are relatively weak, with $\text{Br}\gamma$ only 40% brighter than H_2 2.122 μm .

Comparing our results with HLD99's spectrum for the " H_2 peak," we find that measured line ratios in common between the two studies agree to within the measurement uncertainties. All of the studies of the infrared H_2 lines (cited above) have concluded that there is radiative excitation of the H_2 in BD +30 3639, although probably some collisional modification of the populations is occurring, perhaps due to the effects of high density. In addition, one of us (H. L. D.) has obtained observations of UV absorption lines of H_2 with *FUSE* and *HST*. The *FUSE* band includes a forest of strong Lyman and Werner bands from the $v = 0$ levels of the ground electronic state, while the STIS-FUV MAMA spectral range hosts many strong bands from higher v states that are only populated under radiative excitation. In BD +30 3639, we are able to trace detectable absorption components from excited levels as high as $v = 8, J = 5$ and $v = 5, J = 11$, consistent with models of UV-excited H_2 (Dinerstein & Bowers 2004; H. L. Dinerstein et al. 2006, in preparation).

The molecular content of BD +30 3639 is sufficiently high that it is detected in the CO 1–0 and 2–1 lines (Bachiller et al. 1991; Huggins et al. 1996), although one must be careful to avoid blending or confusion of the $J = 1-0$ line with a high-frequency H I recombination line, $\text{H}38\alpha$ (Bachiller et al. 1992). Huggins et al. (1996) estimate the molecular mass as $8.6 \times 10^{-3} M_\odot$, of which at least $\sim 16\%$ is in the form of fast-moving compact "bullets" (Bachiller et al. 2000). There is also evidence for neutral atomic material, as traced by Na I (Dinerstein et al. 1995) and 21 cm H I line emission (Taylor et al. 1990), although it is possible that some of the latter is ambient material not directly associated with BD +30 3639 (Likkell et al. 1992).

3.4.7. IC 5117

IC 5117 is another bright, compact, apparently young PN. It bears many similarities to Vy 2-2, including a small radio continuum size with subarcsecond bipolarity (Kwok 1985; Miranda et al. 1995) and high densities akin to, if not quite as high as, those in Vy 2-2. Like Vy 2-2 (but unlike NGC 40, SwSt 1, and BD +30 3639), IC 5117 does not have a cool, [WC]-type central star nor the corresponding low-excitation nebular emission-line spectrum (Hyung et al. 2001). The presence of H_2 in IC 5117 has been known for some time (e.g., Geballe et al. 1991), but as of 2000 it had not been included in any of the recent near-infrared spectroscopic surveys of PNs, motivating its inclusion here. The morphology of the H_2 "image" of IC 5117 by Kastner et al. (1996) is not very different from its appearance in continuum images, although the H_2 may have a somewhat greater spatial extent in the north-south direction. We were able to detect the 2.122 μm H_2 line out to an east-west total extent of $8''$, smaller than the detectable emission in the (much brighter) $\text{Br}\gamma$ line, in comparison with a more compact size of $\approx 3.5''$ in the K -band continuum.

IC 5117 was one of the PNs for which we obtained extended spectral coverage. It shows lines of He I , He II , and $[\text{Kr III}]$ in addition to H I , $\text{Br}\gamma$ and H_2 (Fig. 1, *top*). We detected five H_2 lines and set upper limits on two others (Table 4). The main factor limiting our ability to measure weak lines in this object is the strength of the near-infrared continuum, which is in excess of extrapolated contributions from the central star and bound-free emission from the ionized gas, and is probably due to a high color temperature dust component (Zhang & Kwok 1992).

In a recent study, Rudy et al. (2001) presented near-infrared spectra of IC 5117 from 0.8 to 2.4 μm . They report most of the same bright lines as we do here, with generally consistent flux

ratios; some differences (e.g., Rudy et al. [2001] report a lower H_2 2.122 μm -to- $\text{Br}\gamma$ ratio) may be attributable to differences in aperture dimensions and/or seeing. They present line fluxes for H_2 transitions from $v = 1$ only (e.g., their Table 1) and indirectly report upper limits on several transitions from $v = 2$ (e.g., their Fig. 5); whereas in our higher S/N spectrum we detect both the $v = 2-1$ $S(1)$ and $S(3)$ lines (Table 4). Rudy et al. (2001) concluded that the H_2 emission from IC 5117 is collisionally excited, based on comparing their $v = 1-0$ line strengths and $v = 2-1$ upper limits. We discuss the H_2 excitation using our more complete data set in § 4.

We originally believed that we had detected H_2 3–2 $S(3)$ 2.201 μm and interpreted this as implying that the H_2 in IC 5117 must be radiatively excited (Likkell et al. 2000a). We now believe that the apparent feature we saw at 2.201 μm (Dinerstein 2001, Fig. 1) was an artifact caused by overcorrection for telluric absorption. However, it was the spectrum of IC 5117 that initially drew our attention to the 2.199 μm line and led to its identification as $[\text{Kr III}]$. In the present paper we cite an upper limit on the flux of H_2 2.201 μm (Tables 4 and 6) and recalculate the Kr abundance using the revised flux for 2.199 μm (see § 3.3.1).

There is other evidence for molecular material in IC 5117 in the form of CO 1–0 and 2–1 line emission (Huggins & Healy 1989) corresponding to a total molecular mass estimated as 0.012 M_\odot by Huggins et al. (1996) and 0.06 M_\odot by Dayal & Bieging (1996). The H I 21 cm line has also been seen, both in absorption (Taylor et al. 1990) and in emission, along with CO 3–2 (Gussie & Taylor 1995).

4. H_2 LINE RATIOS AND EXCITATION MECHANISM

The two basic mechanisms that can excite H_2 molecules into the energy levels that give rise to the K -band lines, the excited vibrational states ($v \geq 1$) of the ground electronic state, are collisional (thermal) excitation and a radiative fluorescence process initiated by the absorption of far-UV photons of the Lyman and Werner resonance bands. Planetary nebulae in general harbor the agents of both processes, since their central stars are sources of copious UV radiation, and it is believed that shocks are often present and may play a significant role in sculpting their shapes (Kwok 2000; for another view, see Balick & Frank 2002). Since the populations of the excited v, J levels of H_2 are quite different for radiative versus collisional excitation (e.g., Black & van Dishoeck 1987), any observable quantity that has a known dependence on the relative number of atoms in an individual level can provide a means for determining which mechanism is operating. Two examples of such observables are the equivalent widths of absorption lines, sufficiently weak that they are on the linear portion of the curve of growth, and the intensities of optically thin emission lines, such as the near-infrared H_2 lines.

Various procedures have been developed to try to distinguish between collisionally (thermally) and radiatively excited H_2 . Most approaches require information on the populations of at least three (ideally, a larger number of) energy levels. One widely used tool is the excitation-energy diagram, in which the natural logarithms of the N_J/g_J values (where N_J and g_J are the column density and statistical weight of level J , respectively) are plotted against E_J/k , where E_J is the excitation energy of the level. For an isothermal collisionally excited gas, the level populations will be fitted by a straight line of slope T_{kin}^{-1} ; even if the gas is not isothermal, the populations will monotonically decrease with increasing E_J/k under collisional excitation. In contrast, the excitation diagram for radiatively excited H_2 displays a jagged, "sawtooth" pattern, with discontinuities at each step in the value of v (e.g., Hasegawa et al. 1987; Meyer et al. 2001). In addition, the populations of the ortho

(odd J) and para (even J) levels do not necessarily obey the expected ortho/para ratio of 3 that applies for thermal distributions; due to optical depth effects in the UV pumping lines, the value of ortho/para can vary between ~ 1.5 and 3 (e.g., Sternberg & Neufeld 1999), introducing yet another variable whose value must be determined as part of the fit to the data set.

Alternatively, one can formally derive individual values of excitation temperature and compare T_{rot} (inferred from the slopes of the fits to levels with the same v but different J) with T_{vib} (from fits to levels with different values of v). For radiative excitation of H_2 , this yields $T_{\text{vib}} > T_{\text{rot}}$. Both methods are employed in many of the previous studies of infrared H_2 emission from PNs (e.g., Shupe et al. 1998; HLD99; LPH01). The approach used by Davis et al. (2003) is a variant of this method, in which they plot the deviation of the level population ratios from a pure collisional case and extract a value of the shock temperature and amplitude of the radiatively excited component.

In cases in which only limited information is available, ratios among the strongest H_2 lines are often utilized to investigate the excitation mechanism. In particular, the ratios among the 1–0 $S(0)$ 2.223 μm , 2–1 $S(1)$ 2.247 μm , and 1–0 $S(1)$ 2.122 μm lines take on markedly different values for the two excitation mechanisms. For example, in (low-density) radiatively excited H_2 , $F_{2.247}/F_{2.122} \approx 1/2$, while in thermally excited H_2 at any temperature where it is not fully dissociated and/or ionized, the ratio is $\lesssim 0.1$. The ratio $F_{2.223}/F_{2.122}$ is less sensitive, having values of ≈ 0.5 for fluorescence and ≈ 0.2 – 0.3 for shocks of various temperatures (Black & van Dishoeck 1987).

Observational studies have often found line ratios intermediate between the “ideal” cases of pure fluorescence and shocks. One possible interpretation is that both mechanisms are contributing; however, in view of the fact that some PNs are known to have high densities, it seems more likely that collisions are modifying the level populations of an initially radiatively excited H_2 zone. This situation produces a “collisional fluorescent” spectrum (Sternberg & Dalgarno 1989), which is predicted for densities of $\gtrsim 10^4 \text{ cm}^{-3}$. While some of the higher energy levels, $v \geq 3$ – 4 , may still retain their fluorescent population values under these conditions, the emission lines from these levels tend to be weak and are not well represented in the K band. This collisional suppression effect makes the use of the $F_{2.247}/F_{2.122}$ indicator questionable when applied to dense objects. In this context, since PPNs are generally younger and denser than more evolved PNs, the H_2 line ratios of PPNs may tend to be closer to the thermal case due to density effects rather than due to a difference in the basic excitation mechanism.

For most of the objects we observed, we do not have sufficient information to make good use of an excitation-energy diagram or a formal derivation of T_{exc} values. Instead, we simply compare our measurements directly with predictions for representative models of radiative and collisional excitation under conditions appropriate to our sources. Table 6 presents intensity ratios for six of the brightest H_2 lines in the K band, relative to 1–0 $S(1)$ 2.122 μm , from both model predictions and measured values or upper limits for our best-observed sources (Figs. 1 and 2, Tables 4 and 5). We include radiatively excited models covering the likely density range of our observed PNs, ranging from low-density models represented by the “standard” fluorescence model 14 of Black & van Dishoeck (1987) to models for higher densities and stronger UV radiation fields calculated by Draine & Bertoldi (B. Draine 2003, private communication; see also Draine & Bertoldi 1996, 2000). The radiative excitation models are parameterized by nucleon density n (the number density of H nuclei cm^{-3} ; Table 6, col. [2]); intensity of the stellar UV radiation field,

where χ is the ratio to a standard interstellar radiation field (col. [3]); and a representative temperature for the region where the H_2 emission arises (col. [4] lists the kinetic temperature at the point where half of the hydrogen is in molecular form). In addition, we list the ratios given by Black & van Dishoeck (1987) for shocked gas at $T = 1000$ and 2000 K. While the assumption of isothermality is somewhat simplistic, it gives an idea of the range of expected line ratios for collisionally excited H_2 and is sufficient for comparison with our data. The data, including uncertainties in the line ratios (propagated explicitly from the flux uncertainties in Tables 4 and 5), are presented in the last six rows of Table 6.

Inspecting Table 6, it can be seen that we cannot always match up the observations with a unique model. For BD +30 3639, in which we already know from previous studies that the H_2 is radiatively excited but not in the low-density limit (Shupe et al. 1998; HLD99; LPH01), we find that the best match is something close to model D, for which $\log n \approx 5$. The presence of the 3–2 $S(3)$ line and strength of the 2–1 $S(1)$ clearly rule out a shock model here. Likewise, one can probably rule out all radiatively excited models for M 1–13, which appears to be shock excited with a postshock temperature slightly higher than 2000 K. For the other sources, it is more difficult to reach definitive conclusions about the nature of the excitation mechanism. The spectrum of IC 5117 might be produced in shock-excited gas with a temperature intermediate between those of models S1 and S2, as Rudy et al. (2001) concluded, except for a 2.247 μm line that is possibly too strong. However, within our measurement uncertainties for the line ratios, IC 5117 is equally well fitted by model H, the highest density, radiatively excited model included here, or perhaps by a model intermediate between H and F, which gives a better match to the 2.247 μm line.

For the other three PNs in Table 6, we have only one measured line ratio, and upper limits on the others. The nominal ratio of $F_{2.223}/F_{2.122}$ in Vy 2–2 is more consistent with fluorescence than with shocks, although the uncertainty in the flux ratio is sufficiently large that neither mechanism can be excluded. HLD99 also suggested that the H_2 in Vy 2–2 was radiatively excited, but this was partly on the basis of the large apparent $F(2.247)/F(2.122)$ ratio, which was unfortunately due to the misidentification of the line near 2.247 μm as H_2 rather than [Fe III] (see § 3.4.5). However, the estimated measurement uncertainties do not exclude any of the models in Table 6 except the $T = 2000$ K shock (S2), and the upper limit on $F_{2.247}/F_{2.122}$ suggests that thermal excitation is more likely than fluorescence for this source. For SwSt 1, either a dense, radiatively excited model (F or H, as for IC 5117) or a lower temperature shock (model S1) provides a satisfactory match for our limited data. Given the low densities measured in the ionized gas for NGC 40 (§ 3.4.1), it seems more plausible that the H_2 emission is shock excited than UV excited (as suggested by HLD99), but given the weak upper limit on 2.247 μm and the large error bars on $F_{2.223}/F_{2.122}$, neither mechanism can be eliminated as a possibility.

Thus, unfortunately we do not have clear-cut indications of the H_2 excitation mechanism in most of our sources. Previous studies have reached various conclusions about the predominance of one mechanism or the other, but used different analysis approaches on different samples of PNs. In principle, as long as molecular material is bathed by an appropriate UV radiation field, some fluorescent excitation must be occurring (except, perhaps, in PPNs with relatively cool central stars). The question then becomes whether any deviations from pure fluorescence in the observed H_2 line ratios from PNs can be explained by thermalization of the level populations in an originally radiatively excited region, or whether it is also necessary to invoke a shock component. For

TABLE 7
[Fe III] FLUXES AND RATIOS

Model/PN ^a	$\frac{F(2.218)}{F_{\text{Br}\gamma}}$	$\frac{F(2.145)}{F(2.218)}$	$\frac{F(2.243)}{F(2.218)}$	$\frac{n(\text{Fe}^{++})}{n(\text{H}^+)}$ ^b
BP98/K01 ^c ($\log n_e = 4.0$).....	...	0.26	0.81	...
BP98/K01 ($\log n_e = 5.0$).....	...	0.53	1.04	...
K92 ^d ($\log n_e = 4.0$).....	...	0.17	0.29	...
K92 ($\log n_e = 5.0$).....	...	0.34	0.39	...
SwSt 1.....	0.031 ± 0.004	0.51 ± 0.24	0.34 ± 0.12	7.6×10^{-7}
Vy 2-2 ^e	0.022 ± 0.004	0.34 ± 0.13	0.46 ± 0.13	5.4×10^{-7}
Hb 12 ^f	0.010 ± 0.002	0.39 ± 0.22	...	2.4×10^{-7}
Cn 3-1.....	0.013 ± 0.005	3.2×10^{-7}

^a Assumes $T_e = 10,000$ K, but ratios are not sensitive to the value.

^b Assuming $T_e = 10,000$ K, $\log n_e = 5.0$, and populations of K92; derived abundances are $\approx 20\%$ lower using the populations computed by BP98 and K01.

^c Bautista & Pradhan (1998), also Keenan et al. (2001). Both adopt collision strengths from Zhang (1996) and A -values from Nahar & Pradhan (1996).

^d For populations from Keenan et al. (1992) and A -values of Garstang (1957).

^e HLD99 report an unidentified feature with flux $(0.017 \pm 0.010) \times F_{\text{Br}\gamma}$.

^f Luhman & Rieke (1996), measured in their central $3''.5 \times 9''.0$ aperture.

many objects, it is difficult to decide unambiguously between these alternatives unless many H_2 lines are available, although information on morphology and kinematics can lend support to an indicated mechanism. Observations in the far-UV, where the pump lines fall (e.g., Sterling et al. 2005; Dinerstein & Bowers 2004), or the mid-infrared, where the lowest few pure rotational transitions of H_2 lie and the level populations are more likely to indicate the kinetic temperature, may help to address and resolve this puzzle.

5. [Fe III] LINES AND THE DEPLETION OF Fe INTO DUST

5.1. [Fe III] Line Ratios as Density Diagnostics

In § 3.3.2 we briefly discussed our detections of near-infrared lines of [Fe III] in several of our targets. As pointed out by DePoy & Pogge (1994), these lines are also seen in H II regions, where they have the potential to interfere with attempts to measure some of the more popular diagnostic H_2 lines, namely, 2.223 and 2.247 μm (see discussion in § 4). The K -band [Fe III] lines arise from high-excitation energy levels, as do numerous [Fe III] lines in the optical spectral region, which have been seen in many PNs. However, in view of the complex energy-level structure of the Fe ions, use of these lines to derive physical conditions and gas-phase ionic abundances had to wait for the availability of accurate calculations of relevant physical constants, in particular, the cross sections for collisional excitation by electrons. Calculations of these quantities for iron and other elements were undertaken by the IRON Project (Hummer et al. 1993; Nahar & Pradhan 1996).

The [Fe III] lines we detected all belong to the same multiplet, arising from states that are closely spaced in energy. Consequently, although the level populations and resulting line emissivities are sensitive to T_e , the *ratios* among the lines in the multiplet are nearly independent of temperature. They are, however, sensitive to n_e , making them potentially useful as density diagnostics, as are line ratios among some of the optical [Fe III] transitions (K92; Keenan et al. 1993; BP98). The collision strengths among the 17 lowest energy levels of Fe III were calculated by Berrington et al. (1991) and more recently by Zhang (1996). Two independent calculations of the radiative transition probabilities (A -values) were also performed recently, by Nahar & Pradhan (1996) and Quinet (1996).

Using the new values for these constants and including 17 additional energy levels for Fe II, BP98 discussed applications of

the emission lines of [Fe II], [Fe III], and [Fe IV] for deriving properties and abundances of ionized nebulae. In particular, they discussed the use of [Fe III] line ratios, including the K -band multiplet, to constrain n_e (see their Fig. 7). Similar plots were shown—but only for selected optical line pairs—by Keenan et al. (1993), using the older collision strengths from Berrington et al. (1991) and the previously extant A -values from Garstang (1957). Although Keenan et al. (1993) did not present intensity ratios for the near-infrared lines, they can be calculated from the level populations in K92 and an adopted set of A -values. For a more complete set of [Fe III] line intensity ratios, tables are also available in online form in Keenan et al. (2001, hereafter K01). However, note that K01's values for the ${}^3G-{}^3H$ multiplet (or any other ratio in common between the two studies) are identical to those of BP98, since both calculations used exactly the same input parameters: collision strengths from Zhang (1996) and A -values from Nahar & Pradhan (1996). Level populations, which are needed to compute ionic abundances (see § 5.2), were not presented explicitly in the published tables of K01 but were kindly provided to us by F. P. Keenan (2004, private communication).

In Table 7 we list values for two independent line ratios, $F(2.145)/F(2.218)$ and $F(2.243)/F(2.218)$, at representative conditions for the high-density PNs in which we detected these lines. The first two rows of the table give the values from BP98 (which are the same as those in K01, see above) for $\log n_e = 4.0$ and 5.0; in the next two rows we give the ratios predicted using the level populations of K92 and Garstang's A -values.

Finally, we also list in Table 7 our measured ratios of the [Fe III] lines in SwSt 1 and Vy 2-2; in Cn 3-1 we (marginally) detect only the brightest line, [Fe III] 2.218 μm . We also include the only other ratio of these lines we know of for a PN, the ratio of the 2.145 and 2.218 μm lines in Hb 12 as reported by Luhman & Rieke (1996). As discussed in §§ 3.4.4 and 3.4.5, these are relatively dense objects, in which $\log n_e \gtrsim 4.5$. Unfortunately, the lines are weak, particularly 2.145 and 2.243 μm , so the uncertainties in the line ratios are quite large. Nevertheless, inspection of Table 7 shows that while the observed ratios of $F(2.145)/F(2.218)$ are consistent with either the calculations of K92 or BP98 and K01 at the higher density, $\log n_e = 5$, the $F(2.243)/F(2.218)$ ratios appear to be inconsistent with the values predicted by BP98 and K01, even though those used more recent atomic parameters. Instead, they are consistent with the earlier predictions from K92, who used the older collision strengths and

A -values. It would be interesting to obtain [Fe III] line ratios for a larger number of PNs, including some with lower n_e , to test this discrepancy. Luhman et al. (1998) observed near-infrared [Fe III] line ratios in the Orion Bar and Orion S regions and compared them to theoretical values (see their Table 4). The $F(2.145)/F(2.218)$ ratio they find for those regions is smaller than we found for the PNs, indicating a lower density for the Orion region. The Luhman et al. (1998) $F(2.145)/F(2.218)$ and $F(2.243)/F(2.218)$ line ratios are consistent within uncertainty with the K92 values for $\log n_e = 3$ or 4 (an appropriate density for that region), but the $F(2.243)/F(2.218)$ line ratio excludes the BP98/K01 value.

It is not clear why observations of the near-infrared lines do not support the theoretical line ratios. Nahar & Pradhan (1996) compare ratios derived using their own new A -values with calculations assuming Garstang's values and conclude that there are no reasons to prefer one set of A -values over the other. Rodríguez (2002) investigated [Fe III] atomic parameters by comparing optical line ratios from Galactic H II regions with several calculations that adopted different input atomic parameters. Rodríguez found that in general the calculations fit the measured optical line ratios reasonably well and that, if anything, the predictions that used the more recent parameters, those of Zhang (1996) and Quinet (1996), provided a better fit to most (but not all) of the observed line ratios. However, the optical lines arise from different terms in the energy diagram than do the near-infrared lines, so this result does not necessarily prove that the optically preferred parameters provide the best values for interpreting the infrared lines. Further discussion of the [Fe III] spectra and level populations can be found in Sterling et al. (2005).

5.2. Gas-Phase Iron Abundances and Depletions

Since Fe^{++} is an important, and in some cases the major, ionic form of iron in low- and medium-excitation PNs, observations of spectral lines of Fe III are useful for estimating gas-phase iron abundances. The concentration of gaseous iron in the ISM, Fe/H , is typically lower than in the Sun and stars by 1–2 (or even more) orders of magnitude, a fact that is generally interpreted as resulting from the depletion or incorporation of most of the iron nuclei into dust grains (Savage & Sembach 1996 and references therein). This effect is so strong that determinations of ionic abundances such as $n_{\text{Fe}^{++}}/n_{\text{H}^+}$ are used primarily to determine dust “depletion factors.” Such measurements can be obtained, for example, from UV absorption lines from the first few levels of the ion (e.g., Sterling et al. 2005) or from emission lines (e.g., Perinotto et al. 1999; Zhang & Liu 2002).

The ionic abundance ratio can be computed from the observed intensity ratio $F_{2.218 \mu\text{m}}/F_{\text{Br}\gamma}$ (second column of Table 7) and the density-normalized volume emissivities, as was done for [Kr III] in § 3.3.1. We take the physical conditions of $T_e = 10,000$ K and $\log n_e = 5.0$ as representative of SwSt 1, Vy 2-2, and Cn 3-1 (De Marco et al. 2001; MS91; references in Perinotto et al. 1999); so $\epsilon_{\text{Br}\gamma} = 3.4 \times 10^{-27}$ ergs $\text{cm}^3 \text{s}^{-1}$ (using Dopita & Sutherland [2003], as discussed in § 3.3.1; see also Osterbrock 1989, Table 4.4). To compute the emissivity of the $2.218 \mu\text{m}$ line, we used the level populations of K92, since those values seem most consistent with the near-infrared [Fe III] line ratios (see discussion above). This yields $\epsilon_{2.218} = 1.39 \times 10^{-22}$ ergs $\text{cm}^3 \text{s}^{-1}$ for Garstang's A -value of 0.045 s^{-1} . The resulting ionic abundance ratios $n_{\text{Fe}^{++}}/n_{\text{H}^+}$ are given in the last column of Table 7. If we had instead used the level populations of K01 and A -values of Nahar & Pradhan (1996), the ionic abundances would be only 12% lower, which is probably less significant than the uncertainty due to the dependence of the level populations (and hence emissivity) on T_e . Our abundances (Table 7) are consis-

tent with those found from optical region [Fe III] lines for Cn 3-1 (Perinotto et al. 1999) and SwSt 1 (de Freitas Pacheco & Veliz 1987; Sterling et al. 2005). The range of $n_{\text{Fe}^{++}}/n_{\text{H}^+}$ values for the four PNs in Table 7 is similar to those found by Perinotto et al. (1999) for four PNs (including Cn 3-1), and for H II regions studied by Rodríguez (2002).

Since we have not included contributions from other ions of iron, these ionic abundances provide lower limits for the total gas-phase abundances in our PNs. The approximation $n_{\text{Fe}}/n_{\text{H}} \approx n_{\text{Fe}^{++}}/n_{\text{H}^+}$ is best for the PNs with the lowest excitation as indicated by $n_{\text{O}^{++}}/n_{\text{O}^+}$, namely, SwSt 1 and Cn 3-1. The iron depletion factors relative to a solar abundance of $n_{\text{Fe}}/n_{\text{H}} = 2.8 \times 10^{-5}$ (Asplund et al. 2005) range from ≥ -1.57 for SwSt 1 and ≥ -1.72 for Vy 2-2 to ≈ -2 for Hb 12 and Cn 3-1.

We have not attempted to correct our derived values of $n(\text{Fe}^{++})/n(\text{H}^+)$ for other ionization stages, the most important of which are Fe^+ and Fe^{+3} . In SwSt 1, we know that the amount of Fe^+ is only about 4% that of Fe^{++} as measured from either optical emission or UV absorption lines, and the correction for ions higher than Fe^{++} is only $\sim 15\%$ (Sterling et al. 2005). For the “medium-excitation” PN Vy 2-2, which shows prominent [O III] lines, it is likely that a substantial fraction of the gaseous Fe will be in Fe^{+3} , according to the ionization correction factor formula (1) of Rodríguez (2002). If we take the value for the oxygen ionization fraction O/O^+ in Vy 2-2 from the collisionally excited lines [O II] $\lambda\lambda 3727, 3729$ and [O III] $\lambda\lambda 4959, 5007$, the total gas-phase Fe abundance is a factor of 8 ($+0.9$ dex) higher than the value cited in our Table 7; however, a much larger value for O^{++}/H^+ is found from optical O II recombination lines (Wesson et al. 2005). Given the controversy over which are more reliable indicators of ionic abundances, collisionally excited or recombination lines (e.g., see Garnett & Dinerstein 2001; Robertson-Tessi & Garnett 2005), we simply note that the gas-phase Fe abundance in Vy 2-2 is probably larger, and the degree of depletion in dust less extreme, than would be inferred from Fe^{++} alone. Indeed, the gas-phase Fe abundance in Vy 2-2 may well exceed that of SwSt 1.

One noteworthy point is the relatively high gas-phase Fe abundance and correspondingly modest depletion factor for SwSt 1. This updates the value from infrared emission lines cited in Sterling et al. (2005), who found an even higher gaseous Fe^{++} abundance—and lighter depletion factor, possibly consistent with no depletion at all—along the particular line of sight toward the central star, from UV absorption lines. That paper concluded that the dust-to-gas ratio in SwSt 1 was inhomogeneous from place to place within the nebula, which could easily lead to small variations in the inferred Fe abundance when different sets of observations, encompassing different volumes of ionized material, are compared. The reason the refractory element iron is less severely depleted in SwSt 1 than in the cold ISM and in many other ionized nebulae is unclear. Sterling et al. (2005) argued that dust destruction mechanisms such as sputtering by shocks or photoevaporation could not have produced such large differences in depletion factors during the short “lifetime” of this young PN. An alternative explanation is that the initial formation of dust in the outflowing AGB star envelope was nonuniform. Emission-line observations might tend to average out some of the small-scale variations in the depletion factor, but high spatial resolution spectroscopy might potentially be able to track such variations.

Among other near-infrared spectroscopic studies of PNs, LPH01 report detections of K-band [Fe III] lines in a few objects but do not analyze them in detail. Their source list overlaps with ours in only three cases, which do not include the PNs in which we detect [Fe III]. For those objects in which they detect [Fe III], the line

intensities are typically $\sim 1\%$ – 2% that of $\text{Br}\gamma$, which corresponds to gas-phase depletion factors of 50–100 (see above). One of the two objects in which they see unusually strong $[\text{Fe III}]$ 2.218 μm emission, $\sim 4\%$ of $\text{Br}\gamma$, is M 1-78, which is probably an ultra-compact H II region associated with a Population I Wolf-Rayet star, rather than a PN (Gussie 1995). The other, interestingly, is the moderately metal-poor PN DdDm 1 (e.g., Dinerstein et al. 2003), in which one might readily believe that dust formation was less efficient than in more metal-rich, disk population PNs.

6. SUMMARY

We have studied 16 northern planetary nebulae using medium-resolution, long-slit spectroscopy at near-infrared wavelengths. We present K -band spectra for six PNs, NGC 40, M 1-13, SwSt 1, BD +30 3639, Vy 2-2, and IC 5117, in which we detected two or more H_2 lines and present intensities for emission lines in these and the other observed PNs. We compare the measured H_2 line ratios and upper limits to calculated values for different models of the H_2 excitation and address the extent to which we can or cannot distinguish between radiative (photo) excitation and thermal excitation (shocks). We emphasize that in many cases it is difficult to choose conclusively between shocks and radiative excitation, particularly when the gas density is high.

Our observation of the relatively evolved bipolar PN M 1-13 provides spectroscopic confirmation of H_2 emission reported from narrowband imaging (Kastner et al. 1996); H_2 lines dominate the spectrum in the waist of the nebula, with little contamination from emission lines of other species, so the nominal “ H_2 ” filter indeed traces the molecular component. In this PN the spatial extent of the H_2 emission appears to be greater than that of $\text{Br}\gamma$, suggesting that the H_2 emission arises at a shock and/or ionization front, while in several other PNs, the H_2 emission is detected within a smaller region than $\text{Br}\gamma$ emission. We note that the latter situation could result from H_2 emission being produced mainly at the surfaces of self-shielded molecular clumps embedded in the ionized gas, a clumpy photodissociation region, as is seen in nearby, spatially resolved PNs such as the Ring and Helix Nebulae.

We report detections of $[\text{Kr III}]$ 2.199 μm in NGC 40, SwSt 1, and IC 5117. This, as well as several $[\text{Fe III}]$ lines that we detect in SwSt 1 and Vy 2-2 (and perhaps Cn 3-1), can blend or interfere with the measurement of H_2 lines often used to diagnose the H_2 excitation mechanism. This is a more serious effect than has been commonly recognized, since the gas-phase elemental abundances

of Kr and Fe may be elevated under certain circumstances by factors of a few to ~ 10 . We find evidence for a somewhat enhanced abundance of Kr in IC 5117, which is uncertain due to a large ionization correction, whereas in NGC 40, the *minimum* enrichment factor is about 7 relative to the solar Kr/H value. This can be attributed to enrichment by neutron-capture nucleosynthesis, followed by convective dredge-up of s -processed material from the deep interior during the thermally pulsing AGB phase.

The $[\text{Fe III}]$ lines that we see in SwSt 1 and Vy 2-2 have fluxes of $\approx 2\%$ of $\text{Br}\gamma$. We compare their observed ratios with predicted values computed using different sets of atomic parameters (collision strengths and transition probabilities). There appear to be some discrepancies between the predictions employing the most recent parameters and the observed strengths of the near-infrared lines, which belong to the $^3G-^3H$ multiplet. We estimate gas-phase abundances of Fe^{++} for four objects, finding values comparable to those determined from optical emission $[\text{Fe III}]$ lines in H II regions and PNs. Some of the PNs show evidence for less severe depletion of Fe into dust grains than is the case in the ISM. This may be the result of partial dust destruction or less efficient condensation during the dust formation phase. Additional and higher S/N observations of $[\text{Fe III}]$ lines in PNs and H II regions with a range in n_e will be helpful in testing the accuracy of the atomic constants and improving their reliability as indicators of density and dust-to-gas ratios for ionized nebulae.

This paper is based on data taken at the McDonald Observatory of the University of Texas at Austin. We are grateful for the tireless assistance of the McDonald observing support staff. We acknowledge the contributions of former University of Wisconsin–Eau Claire students Jessica Bruch, for pursuing the analysis of the iron line data, and Paul R. Martin, for assistance with the data reduction. B. Draine provided helpful advice and theoretical results on H_2 line ratios in PDRs. O. De Marco kindly shared additional details on the infrared spectrum of SwSt 1. We also acknowledge helpful discussions with N. C. Sterling on the analysis of the $[\text{Kr III}]$ and $[\text{Fe III}]$ lines and private communication with F. P. Keenan, who provided additional information on the Fe III level populations. This research was supported by NSF grants AST 97-31156 and 04-06809 to H. L. D. and by grants to L. L. from the Office of Research and Sponsored Programs at the University of Wisconsin–Eau Claire. This research made use of NASA’s Astrophysics Data System.

REFERENCES

- Aaquist, O. B., & Kwok, S. 1990, *A&AS*, 84, 229
 Aleman, I., & Gruenwald, R. 2004, *ApJ*, 607, 865
 Asplund, M., Grevesse, N., & Sauval, A. J. 2005, in *ASP Conf. Proc.* 336, *Cosmic Abundances as Records of Stellar Evolution and Nucleosynthesis*, ed. F. N. Bash & T. G. Barnes (San Francisco: ASP), 25
 Bachiller, R., Forveille, T., Huggins, P. J., Cox, P., & Maillard, J. P. 2000, *A&A*, 353, L5
 Bachiller, R., Huggins, P. J., Cox, P., & Forveille, T. 1991, *A&A*, 247, 525
 Bachiller, R., Huggins, P. J., Martín-Pintado, J., & Cox, P. 1992, *A&A*, 256, 231
 Balick, B., & Frank, A. 2002, *ARA&A*, 40, 439
 Bautista, M. A., & Pradhan, A. K. 1998, *ApJ*, 492, 650 (BP98)
 Beckwith, S., Gatley, I., & Persson, S. E. 1978, *ApJ*, 219, L33
 Berrington, K. A., Zeippen, C. J., Le Dourneuf, M., Eissner, W., & Burke, P. G. 1991, *J. Phys. B*, 24, 3467
 Biémont, E., & Hansen, J. E. 1986, *Phys. Scr.*, 34, 116
 Black, J., & van Dishoeck, E. F. 1987, *ApJ*, 322, 412
 Blöcker, T. 1995, *A&A*, 299, 755
 Busso, M., Gallino, R., & Wasserburg, G. J. 1999, *ARA&A*, 37, 239
 Christianto, H., & Seaquist, E. R. 1998, *AJ*, 115, 2466
 Corradi, R. L. M., & Schwarz, H. E. 1995, *A&A*, 293, 871
 Davis, C. J., Smith, M. D., Stern, L., Kerr, T. H., & Chiar, J. E. 2003, *MNRAS*, 344, 262
 Dayal, A., & Biegging, J. H. 1996, *ApJ*, 472, 703
 de Freitas Pacheco, J. A., & Veliz, J. G. 1987, *MNRAS*, 227, 773
 DePoy, D. L., & Pogge, R. W. 1994, *ApJ*, 433, 725
 DePoy, D. L., & Shields, J. C. 1994, *ApJ*, 422, 187
 De Marco, O., Crowther, P. A., Barlow, M. J., Clayton, G. C., & de Koter, A. 2001, *MNRAS*, 328, 527
 Dinerstein, H. L. 1991, *PASP*, 103, 861
 ———. 2001, *ApJ*, 550, L223
 ———. 2004a, in *ASP Conf. Proc.* 313, *Asymmetrical Planetary Nebulae III*, ed. M. Meixner et al. (San Francisco: ASP), 116
 ———. 2004b, in *Origin and Evolution of the Elements*, ed. A. McWilliam & M. Rauch (Pasadena: Carnegie Obs.), 15
 Dinerstein, H. L., & Bowers, C. W. 2004, in *ASP Conf. Proc.* 313, *Asymmetrical Planetary Nebulae III*, ed. M. Meixner et al. (San Francisco: ASP), 347
 Dinerstein, H. L., Lester, D. F., Carr, J. S., & Harvey, P. M. 1988, *ApJ*, 327, L27
 Dinerstein, H. L., Richter, M. J., Lacy, J. H., & Sellgren, K. 2003, *AJ*, 125, 265
 Dinerstein, H. L., Sneden, C., & Uglum, J. 1995, *ApJ*, 447, 262

- Dopita, M. A., & Sutherland, R. S. 2003, *Astrophysics of the Diffuse Universe* (Berlin: Springer)
- Draine, B. T. 2004, in *The Cold Universe*, ed. A. W. Blain, F. Combes, & B. T. Draine (Berlin: Springer), 213
- Draine, B. T., & Bertoldi, F. 1996, *ApJ*, 468, 269
- . 2000, in *Molecular Hydrogen in Space*, ed. F. Combes & G. Pineau des Forêts (Cambridge: Cambridge Univ. Press), 131
- Ekberg, J. O. 1993, *A&AS*, 101, 1
- Feibelman, W. A. 1993, *PASP*, 105, 595
- Flower, D. R., Goharji, A., & Cohen, M. 1984, *MNRAS*, 206, 293
- García-Hernández, D. A., Manchado, A., García-Lario, P., Domínguez-Tagle, C., Conway, G. M., & Prada, F. 2002, *A&A*, 387, 955
- Garnett, D. G., & Dinerstein, H. L. 2001, *ApJ*, 558, 145
- Garstang, R. H. 1957, *MNRAS*, 117, 393
- Geballe, T. R., Burton, M. G., & Isaacman, R. 1991, *MNRAS*, 253, 75
- Goldshmidt, O., & Sternberg, A. 1995, *ApJ*, 439, 256
- Górný, S. K., Schwarz, H. E., Corradi, R. L. M., & Van Winckel, H. 1999, *A&AS*, 136, 145
- Graham, J. R., Herbst, T. M., Matthews, K., Neugebauer, G., Soifer, B. T., Serabyn, E., & Beckwith, S. 1993a, *ApJ*, 408, L105
- Graham, J. R., Serabyn, E., Herbst, T. M., Matthews, K., Neugebauer, G., Soifer, B. T., & Beckwith, S. 1993b, *AJ*, 105, 250
- Gruenwald, R., & Viegas, S. M. 2000, *ApJ*, 543, 889
- Guerrero, M. A., Villaver, E., Manchado, A., García-Lario, P., & Prada, F. 2000, *ApJS*, 127, 125
- Gussie, G. T. 1995, *Proc. Astron. Soc. Australia*, 12, 31
- Gussie, G. T., & Taylor, A. R. 1995, *MNRAS*, 273, 801
- Harrington, J. P., Lame, N. J., White, S. M., & Borkowski, K. J. 1997, *AJ*, 113, 2147
- Hasegawa, T. I. 2003, in *IAU Symp. 209, Planetary Nebulae*, ed. S. Kwok, M. Dopita, & R. Sutherland (San Francisco: ASP), 249
- Hasegawa, T., Gatley, I., Garden, R. P., Brand, P. W. J. L., Ohishi, M., Hayashi, M., & Kaifu, N. 1987, *ApJ*, 318, L77
- Hasegawa, T. I., Volk, K., & Kwok, S. 2000, *ApJ*, 532, 994
- Hollenbach, D., & Natta, A. 1995, *ApJ*, 455, 133
- Hora, J. L., Latter, W. B., & Deutsch, L. 1999, *ApJS*, 124, 195 (HLD99)
- Hrivnak, B. J. 2003, in *IAU Symp. 209, Planetary Nebulae*, ed. S. Kwok, M. Dopita, & R. Sutherland (San Francisco: ASP), 113
- Huggins, P. J., Bachiller, R., Cox, P., & Forveille, T. 1996, *A&A*, 315, 284
- Huggins, P. J., Forveille, T., Bachiller, R., Cox, P., Ageorges, N., & Walsh, J. R. 2002, *ApJ*, 573, L55
- Huggins, P. J., & Healy, A. P. 1989, *ApJ*, 346, 201
- Hummer, D. G., Berrington, K. A., Eissner, W., Pradhan, A. K., Saraph, H. E., & Tully, J. A. 1993, *A&A*, 279, 298
- Hyung, S., Aller, L. H., Feibelman, W. A., & Lee, S.-J. 2001, *ApJ*, 563, 889
- Jacoby, G. J., Quigley, R. J., & Africano, J. L. 1987, *PASP*, 99, 672
- Kaler, J. B., & Jacoby, G. J. 1989, *ApJ*, 345, 871
- Kastner, J. H., Gatley, I., Merrill, K. M., Probst, R. G., & Weintraub, D. A. 1994, *ApJ*, 421, 600
- Kastner, J. H., Weintraub, D. A., Gatley, I., Merrill, K. M., & Probst, R. G. 1996, *ApJ*, 462, 777
- Keenan, F. P., Aller, L. H., Hyung, S., Conlon, E. S., & Warren, G. A. 1993, *ApJ*, 410, 430
- Keenan, F. P., Aller, L. H., Ryans, R. S. I., & Hyung, S. 2001, *Proc. Natl. Acad. Sci.*, 98, 9476 (K01)
- Keenan, F. P., Berrington, K. A., Burke, P. G., Zeippen, C. J., Le Dourneuf, M., & Clegg, R. E. S. 1992, *ApJ*, 384, 385 (K92)
- Köppen, J., & Preite-Martínez, A. 1991, *A&A*, 248, 191
- Kwok, S. 1985, *AJ*, 90, 49
- . 2000, *The Origin and Evolution of Planetary Nebulae* (Cambridge: Cambridge Univ. Press), chap. 13
- Kwok, S., Purton, C. R., & Keenan, D. W. 1981, *ApJ*, 250, 232
- Latter, W. B., Dayal, A., Biegging, J. H., Meakin, C., Hora, J. L., Kelly, D. M., & Tielens, A. G. G. M. 2000, *ApJ*, 539, 783
- Latter, W. B., Kelly, D. M., Hora, J. L., & Deutsch, L. K. 1995, *ApJS*, 100, 159
- Lester, D. F., Hill, G. J., Doppmann, G., & Froning, C. S. 2000, *PASP*, 112, 384
- Likkel, L., Bartig, K., Dinerstein, H. L., & Lester, D. F. 2000a, *BAAS*, 32, 1400
- . 2002, *BAAS*, 34, 1254
- Likkel, L., Dinerstein, H. L., Lester, D. F., Bruch, J., & Bartig, K. 2004, in *ASP Conf. Proc. 313, Asymmetrical Planetary Nebulae III*, ed. M. Meixner et al. (San Francisco: ASP), 351
- Likkel, L., Gussie, G. T., Taylor, A. R., & Dewdney, P. E. 1992, *AJ*, 103, 538
- Likkel, L., Kindt, A., Dinerstein, H. L., & Lester, D. F. 2000b, in *ASP Conf. Proc. 199, Asymmetrical Planetary Nebulae II*, ed. J. H. Kastner, N. Soker, & S. Rappaport (San Francisco: ASP), 333
- Luhman, K. L., Engelbracht, C. W., & Luhman, M. L. 1998, *ApJ*, 499, 799
- Luhman, K. L., & Rieke, G. H. 1996, *ApJ*, 461, 298
- Lumsden, S. L., Puxley, P. J., & Hoare, M. G. 2001a, *MNRAS*, 328, 419 (LPH01)
- . 2001b, *MNRAS*, 320, 83
- Lutz, D., Krabbe, A., & Genzel, R. 1993, *ApJ*, 418, 244
- Maloney, P. R., Hollenbach, D. J., & Tielens, A. G. G. M. 1996, *ApJ*, 466, 561
- Meaburn, J., Lopez, J. A., Bryce, M., & Mellema, G. 1996, *A&A*, 307, 579
- Meyer, D. M., Lauroesch, J. T., Sofia, U. J., Draine, B. T., & Bertoldi, F. 2001, *ApJ*, 553, L59
- Miranda, L. F., & Solf, J. 1991, *A&A*, 252, 331 (MS91)
- Miranda, L. F., Torrelles, J. M., & Eiroa, C. 1995, *ApJ*, 446, L39
- Nahar, S. N., & Pradhan, A. K. 1996, *A&AS*, 119, 509
- Natta, A., & Hollenbach, D. 1998, *A&A*, 337, 517
- O'Dell, C. R., Balick, B., Hajian, A. R., Henney, W. J., & Burkert, A. 2002, *AJ*, 123, 3329
- O'Dell, C. R., Henney, W. J., & Ferland, G. J. 2005, *AJ*, 130, 172
- Osterbrock, D. E. 1989, *Astrophysics of Gaseous Nebulae and Active Galactic Nuclei* (Mill Valley: University Science Books)
- Payne, H. E., Phillips, J. A., & Terzian, Y. 1988, *ApJ*, 326, 368
- Perinotto, M., Bencini, C. G., Pasquali, A., Manchado, A., Rodríguez Espinosa, J. M., & Stanga, R. 1999, *A&A*, 347, 967
- Pottasch, S. R., Bernard-Salas, J., Beintema, W. A., & Feibelman, W. A. 2003, *A&A*, 409, 599
- Quinet, P. 1996, *A&AS*, 116, 573
- Ramsay, S. K., Chrysostomou, A., Geballe, T. R., Brand, P. W. J. L., & Mountain, M. 1993, *MNRAS*, 263, 695
- Redman, M. P., Viti, S., Cau, P., & Williams, D. A. 2003, *MNRAS*, 345, 1291
- Robertson-Tessi, M., & Garnett, D. G. 2005, *ApJS*, 157, 371
- Rodríguez, M. 2002, *A&A*, 389, 556
- Rudy, R. J., Lynch, D. K., Mazuk, S., Puetter, R. C., & Dearborn, D. S. P. 2001, *AJ*, 121, 362
- Sabbadin, F., Cappellaro, E., Benetti, S., Turatto, M., & Zanin, C. 2000, *A&A*, 355, 688
- Sahai, R., & Trauger, J. T. 1998, *AJ*, 116, 1357
- Savage, B. D., & Sembach, K. R. 1996, *ARA&A*, 34, 279
- Schöning, T. 1997, *A&AS*, 122, 277
- Seaquist, E. R., & Davis, L. E. 1983, *ApJ*, 274, 659
- Sellgren, K., Werner, M. W., & Dinerstein, H. L. 1983, *ApJ*, 271, L13
- Shupe, D. L., Armus, L., Matthews, K., & Soifer, B. T. 1995, *AJ*, 109, 1173
- Shupe, D. L., Larkin, J. E., Knop, R. A., Armus, L., Matthews, K., & Soifer, B. T. 1998, *ApJ*, 498, 267
- Smith, H. A., Larson, H. P., & Fink, U. 1981, *ApJ*, 244, 835
- Speck, A. K., Meixner, M., Fong, D., McCullough, P. R., Moser, D. E., & Ueta, T. 2002, *AJ*, 123, 346
- Speck, A. K., Meixner, M., Jacoby, G. H., & Knezek, P. M. 2003, *PASP*, 115, 170
- Sterling, N. C., & Dinerstein, H. L. 2004, in *ASP Conf. Proc. 313, Asymmetrical Planetary Nebulae III*, ed. M. Meixner et al. (San Francisco: ASP), 410
- . 2005a, in *ASP Conf. Proc. 336, Cosmic Abundances as Records of Stellar Evolution and Nucleosynthesis*, ed. T. G. Barnes & F. N. Bash (San Francisco: ASP), 367
- . 2005b, *Rev. Mex. AA Ser. Conf.*, 23, 1
- Sterling, N. C., Dinerstein, H. L., & Bowers, C. W. 2002, *ApJ*, 578, L55
- Sterling, N. C., Dinerstein, H. L., Bowers, C. W., & Redfield, S. 2005, *ApJ*, 625, 368
- Sternberg, A., & Dalgarno, A. 1989, *ApJ*, 338, 197
- Sternberg, A., & Neufeld, D. A. 1999, *ApJ*, 516, 371
- Taylor, A. R., Gussie, G. T., & Pottasch, S. R. 1990, *ApJ*, 351, 515
- Tielens, A. G. G. M. 1993, in *IAU Symp. 155, Planetary Nebulae*, ed. R. Weinberger & A. Acker (Dordrecht: Kluwer), 155
- Treffers, R. R., Fink, U., Larson, H. P., & Gautier, T. N., III. 1976, *ApJ*, 209, 793
- Tylenda, R. 1986, *A&A*, 156, 217
- Vicini, B., Natta, A., Marconi, A., Testi, L., Hollenbach, D., & Draine, B. T. 1999, *A&A*, 342, 823
- Wesson, R., Liu, X.-W., & Barlow, M. J. 2005, *MNRAS*, 362, 424
- Zhang, C. Y., & Kwok, S. 1992, *ApJ*, 385, 255
- Zhang, H. 1996, *A&AS*, 119, 523
- Zhang, Y., & Liu, X.-W. 2002, *MNRAS*, 337, 499
- Zuckerman, B., & Gatley, I. 1988, *ApJ*, 324, 501